BIG ACTUATED THREE-MIRROR ANASTIGAMAT NETWORK

by

Ryan Andrew Bunyard

_____

A Thesis Submitted to the Faculty of the

JAMES C. WYANT COLLEGE OF OPTICAL SCIENCES

In Partial Fulfillment of the Requirements

For the Degree of

MASTER OF SCIENCE
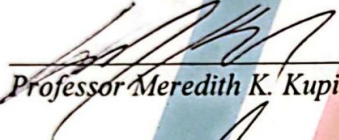
In the Graduate College

THE UNIVERSITY OF ARIZONA

2023

THE UNIVERSITY OF ARIZONA
GRADUATE COLLEGE

As members of the Master's Committee, we certify that we have read the thesis prepared by **Ryan Bunyard**, titled *Big Actuated Three Mirror Anastigmat Network* and recommend that it be accepted as fulfilling the thesis requirement for the Master's Degree.

_____   Date: 12/11/23
Professor Daewook Kim

_____   Date: 12/11/23
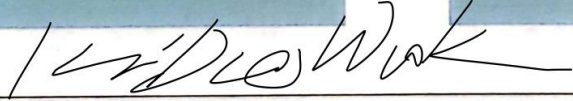*Professor Meredith K. Kupinski*

_____   Date: 12/11/23
Professor Heejoo Choi

Final approval and acceptance of this thesis is contingent upon the candidate's submission of the final copies of the thesis to the Graduate College.

I hereby certify that I have read this thesis prepared under my direction and recommend that it be accepted as fulfilling the Master's requirement.

_____   Date: 12/11/23
Professor Daewook Kim
Master's Thesis Committee Chair
Wyant College of Optical Sciences

Acknowledgements

Foremost I would like to thank my wonderful wife, Melinda, for her unwavering support through this journey. It has been a long and difficult journey, and I thank you for being by my side every step of the way. I could not have achieved this goal without you being there for me through thick and thin. I love you.

I'd like to thank my family for encouraging me through this entire process. You have been a light during darkness and uncertainty. I am happy that you are there to share this experience.

I would also like to thank Dr. Daewook Kim for his technical guidance in this entire process. I could not have done it without you. I also appreciate all that you do for the LOFT group and your students. You are a true blessing in my life and in the lives of all the people with whom you interact.

Thank you as well to Joshua McDonald for being a steadfast friend from the undergraduate program to the present. You have been, and continue to be, my best friend. I appreciate having walked through this scholastic journey with you.

Dedication

For Melinda. You are my love and my life. I could not have done this without you.

Table of Contents

List of Figures

List of Tables

List of Equations

Abstract

The success of the James Webb Space Telescope (JWST) ignited the scientific community to research a new era of telescope development. Furthermore, it is reasonable to assume that there will be more missions of a similar nature and purpose in the future. From now until the time the JWST is retired from service, updates in telescope, mounting, deployment, and even launch technology capabilities will be realized. This thesis outlines the opto-mechanical packaging of an Off-Axis -Three Mirror Anastigmat (OA-TMA). This optical system is designed to have an entrance pupil diameter of 150 mm, a focal length of 407.185 mm, and a 2.1^0x2.05^0 Field of View (FOV). The operational imaging waveband for this system is in the mid-wave infrared band. The selected camera for this system is the Teledyne Neutrino QX[1]. Because the optical system is obscuration free, it results in a different packaging solution for space operation than that of the JWST. The primary requirement of this system is to fold into a smaller volume than its deployment configuration. The novel packaging method in this study resulted in a 66.7% reduction of volume.

1. Introduction

Telescopes have long been in use for scientific and recreational purposes. These tools are instrumental in making ground-breaking discoveries and inspiring many minds to join scientific fields. The most advanced of these are space telescopes. There are two kinds of space telescopes: ground-based and space-borne. Ground based telescopes are huge undertakings of science and engineering. They are installed at high elevations, such as Mauna Kea – home of the Keck Observatory. This allows them to be remote, so the devices are unimpeded by light pollution from big cities, extra vibrations from general activities that are associated with a large

group of people concentrated in single area, and they have much less atmosphere through which they must image.

1.1 Historical Review of Telescopes

Famous examples of these ground-based optical systems include the Giant Magellan Telescope (GMT), the Extremely Large Telescope (ELT), and the Large Binocular Telescope (LBT). These impressive systems All have one common limitation: they are based on the ground. Earth's atmosphere has strong absorption characteristics for infrared wavelengths. These ground-based observatories can and do operate in the IR, but space-based observatories do not share this limitation. As a result, they exist for the purpose of making infrared observations of the sky. The scientific community is interested in the observations made by space-based telescopes because they help in gaining an understanding of the early universe.

1.1.1 Space Telescopes

The creation of space-based observatories happened because they have the advantage of imaging through space instead of Earth's atmosphere. The first of these observatories was the *Infrared Astronomical Satellite* (Neugebauer et al. 1984). This observatory was able to discover many kinds of astronomical objects including distant galaxies, planetary disks, asteroids, and intergalactic cirrus (Houck et al. 1984). There have been many other space observatories that make observations in the infrared spectrum. Notably, the *Spitzer* space telescope is equipped with an Infrared Array Camera (IRAC) has made observations of high-z galaxies using a 4-channel camera that images 3.6, 4.5, 5.8, 8.0 µm wavelengths (Fazio et al. 2004). Celestial phenomena of great interest include interstellar medium, the formation of stars, planetary disks, and the birth and evolution of galaxies, and they are in the mid-wave infrared and long-wave infrared bands (Onaka et al. 2007).

1.1.2 IR Telescopes

The *Akari* satellite had an Infrared Camera (IRC) that made observations of objects of interest in the 1.8 – 26.5 µm waveband. The *Wide-field Infrared Survey Explorer* is another example of an all-sky IR imager that possesses 4 channels imaging at the following respective wavelengths: 3.3, 4.7, 12, 23 µm (Duval et al. 2004). There are other space telescopes that cover both the visible and the infrared wavebands including the JWST which covers 0.6-28 µm wavelengths (Rivta et al. 2012). There is a major common element to the listed space-based observatories: they are all on-axis systems.

1.1.3 Historical Limitations

On-axis systems consist of simpler systems to design and manufacture in contrast to off-axis systems. These on-axis systems possess symmetry that is especially useful in the correction of aberrations. However, they tend to have narrow fields of view because the secondary mirror needs to be smaller in diameter in comparison to the primary mirror due to the back of the secondary mirror for an on-axis telescope systems acts as a large obscuration. This only reduces the amount of light captured and reduces the possible field of view. Refractive systems do not, typically, suffer from the same obscuration and narrow field of view problems. The Multi-purpose Infra-Red Imaging System is a five-element system with a full field of view of 3.67^0x3.67^0 and sees wavelengths from 0.9-2.0 µm (Park et al. 2020). The refractive system described here can observe Paschen-α emission lines along the Galactic plane and infrared cosmic background (Ree et al. 2010; Han et al. 2014). While refractive systems do not suffer from loss resulting from an on-axis obscuration, they do have chromatic effects from their refractive surfaces.

1.2 Motivation of the Three-Mirror Anastigmat Design

The motivation behind using an all-reflective off-axis freeform OA-TMA system is to alleviate the obscuration and narrow field of view limitation of a traditional on-axis all reflective telescope system, and it can operate in a wider band than the all-refractive system given the proper selection of sensors. To be capable of using such a telescope system, a novel optomechanical packaging approach is necessary. The process of deploying the telescope will also be novel.

1.2.1 Proposed Solution of Off-Axis Reflective Telescopes

This study defines an all-reflective optical design meant for off-axis imaging system with realistic tolerances. The optical design is analyzed and optimized for linear astigmatism, and the purpose of the thesis is to design a viable solution for packaging and deployment for an OA-TMA in space to perform observation tasks.

2. Optical Design of the Off-Axis Three-Mirror Anastigmat Telescope

This system is an OA-TMA. This kind of optical telescope is an off-axis confocal three-mirror-system. The optical layout of the system is shown in Figure 1.
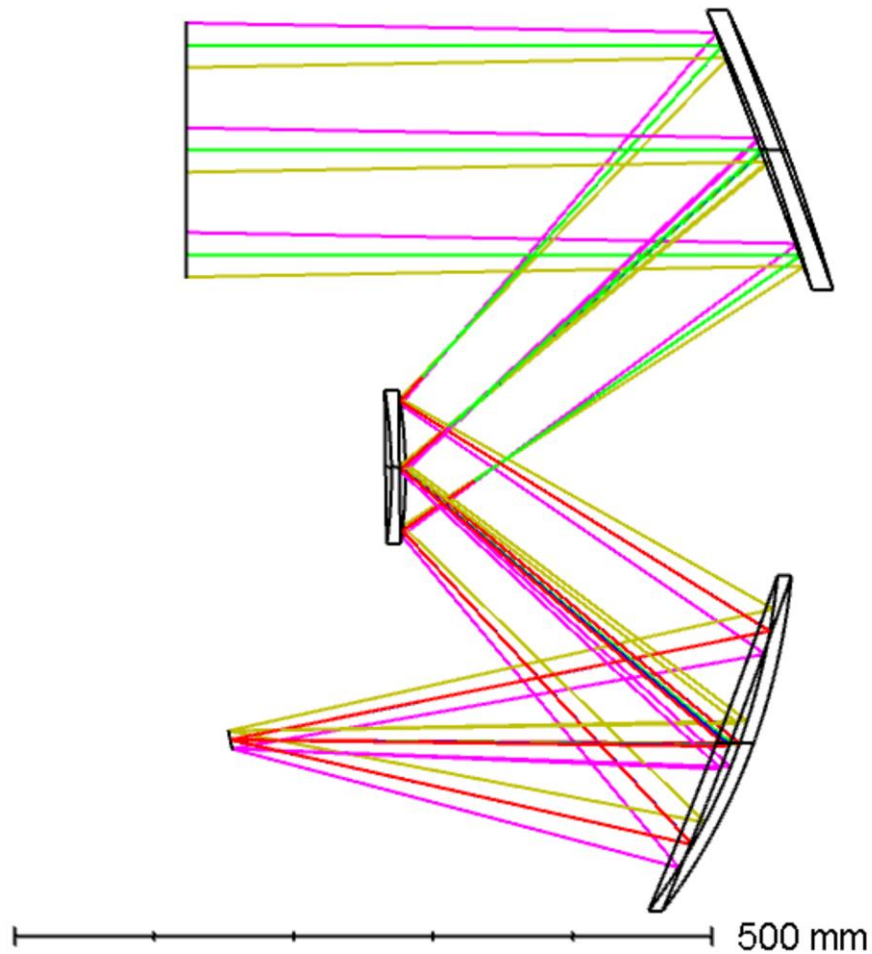
Figure 1: The optical layout of the OA-TMA off axis telescope system.

The system, as seen in Figure 1, is designed to be free of linear astigmatism. The optical path for this system is shown by the colored lines in Figure 1. Each color represents a different field angle. The base-line confocal off-axis design has a mirror surface of a concave mirror that is parabolic for the primary mirror (M1). The secondary mirror (M2) is ellipsoidal and convex. Finally, the tertiary mirror (M3) is ellipsoidal and concave. M1 and M2 share a common focus.

M2 and M3 share a common focus as well. This means that M2 has two shared foci, one with M1 and the other with M3. The confocal nature of this design is shown in Figure 3.

The incident angles on the mirror depicted in Figure 3 are denoted as i_1, i_2, and i_3. The inter mirror distances are denoted as l and l' for each surface. These distances are also known as despace. These despace terms are calculated accurately to satisfy the linear-astigmatism-free condition with the prescribed angles of incidence. This condition is expressed in Equation (1) (Chang 2013).

$$\frac{l'_2 l'_3}{l_2 l_3}\tan(i_1) + \left(1 + \frac{l'_2}{l_2}\right)\frac{l'_3}{l_3} tan(i_2) + \left(1 + \frac{i'_3}{l_3}\right)1 \tan(i_3) = 0 \qquad (1)$$

The parameters l_2 and l_3 and l'_2 and l'_3 in Equation 1 are the front and rear focal lengths of each mirror respectively. They are also depicted in Figure 3. Table 1 shows the calculated values from this operation, and these values were used as the starting point to design the system. The final optimization was done using the Ansys Zemax optimizer.

2.1 Mid-Wave Infrared (MWIR) Camera

The system was optimized to the 3 µm to 5 µm wavelength range as that is roughly the operational waveband of the Teledyne FLIR Neutrino QX camera that was selected for this system (FLIR). According to the spot diagrams shown in Figure 4, this system produces an optimal spot size that is under the diffraction limit, and the spot will take up about 2 pixels on the camera.
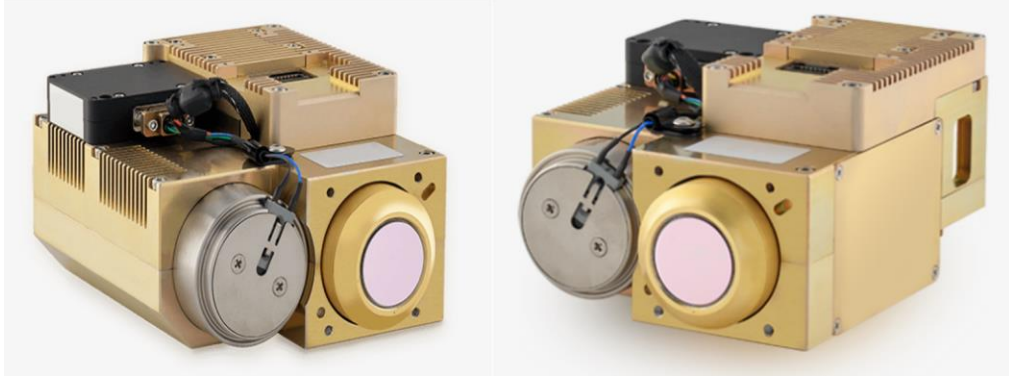
Figure 2: Neutrino MWIR Camera

2.1.1 MWIR Detector Characteristics

The specified camera images wavelengths from about 3 µm to 5 µm. The sensor has a pixel pitch of 10 µm with a resolution of 2048x1536. This indicates that the selected camera has a sensor size of 20.48x15.36 mm. The physical dimensions of the camera are 13.4 cm x 7.0 cm x 10.3 cm. The mass of the camera is 1970 grams. The detector material is InSb. The camera's integration time is programmable from 0.01 to 16 ms (FLIR).

2.2 Optical Design Parameters

Each mirror's reflective surface would be gold coated for optimal strong performance in the MWIR band. The gold coating used for the mirrors on the JWST is 97.9% reflective by requirement but was measured to be 98.5-98.8% for wavelengths spanning 2 µm to 20 µm (Ritva et al. 2012).

Table 1: OA-TMA Parameters

Parameter	Value
l_2	625 mm
l_3	781.19 mm
l'_3	413.50 mm
i_1	16°
i_2	22°
i_3	11.38°
EPD	150 mm
EFL	407.185 mm
FFOV	$2.1^{\circ} \times 2.05^{\circ}$

The same kind of coating procedure would be used to coat the mirrors for this specific system. The mirrors would be coated with gold on the surface of the substrate, and then the gold coating would receive a thin SiO_2 to protect the coating from any scratches or contaminants during the integration and test process (Riveta et al. 2012).
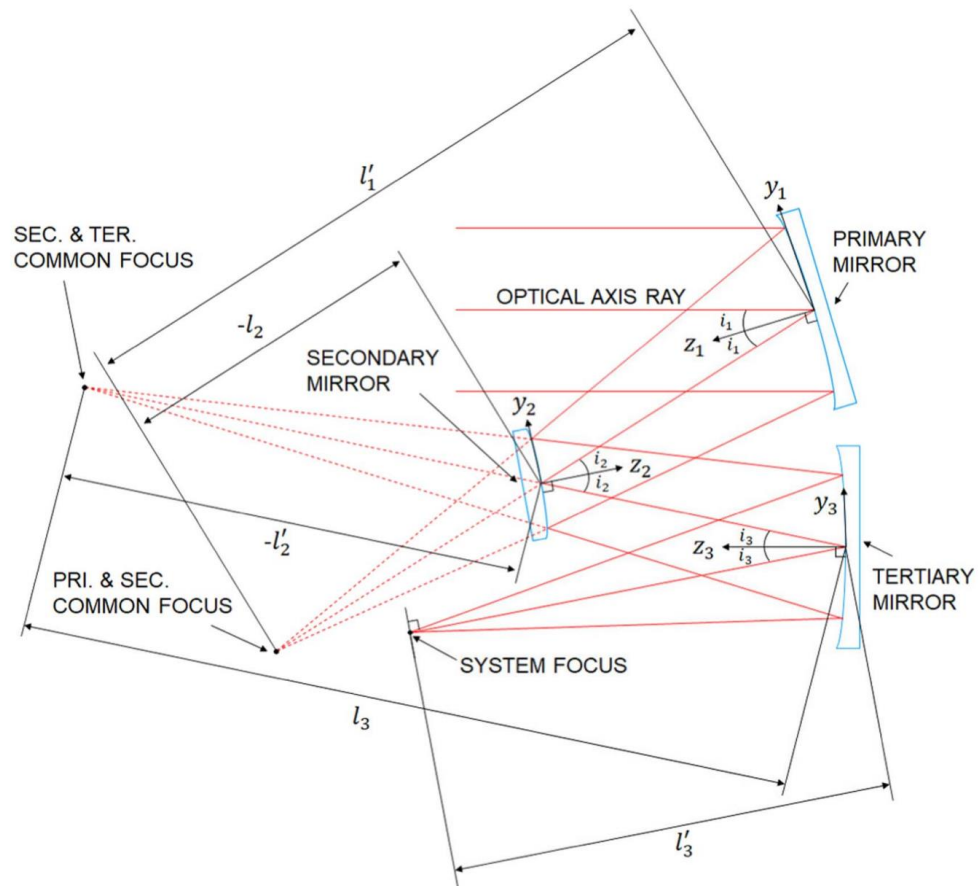
Figure 3: Optical layout diagram showing the parameters for achieving the linear condition.

In Figure 3 the optical path is shown in solid red lines while the shared virtual foci are shown as dotted lines (Park et al. 2020).

3. Optical Performance Optimization and Analysis

The entrance pupil diameter (EPD) of the system is 150 mm. The focal length of this system as designed is 407.185 mm. The full field of view (FFOV) for this system is $2.1^0\text{x}2.05^0$. The system aperture stop is located at the secondary mirror. This accommodates the large primary and secondary mirrors. The mirrors are all freeform to optimize for higher-order

aberrations. These freeform mirrors also satisfy the linear-astigmatism-free condition thus

correcting linear astigmatism. The sensor is tilted to correct for field curvature.

3.1 Airy Disk and Spot Diagram

For the entirety of the operational waveband, the design is diffraction limited. The system

is diffraction limited across four of the five fields. The one field where the system performance is

not at the diffraction limit performs near the diffraction limit and is still acceptable for the

Neutrino QX. Figure 4 shows the spot diagram for all fields and wavelengths in the system. The

black circle denotes the Airy Disk for this system at the primary wavelength in the optical model

which is 4 µm.

Figure 4: A spot diagram of the OA-TMA confocal system.

19

3.2 Sensitivity Analysis with Monte Carlo Simulation

The optical performance of optical systems degrades when they are manufactured because of manufacturing errors. The sensitivity to these errors is evaluated in by tolerance and sensitivity analysis (Wa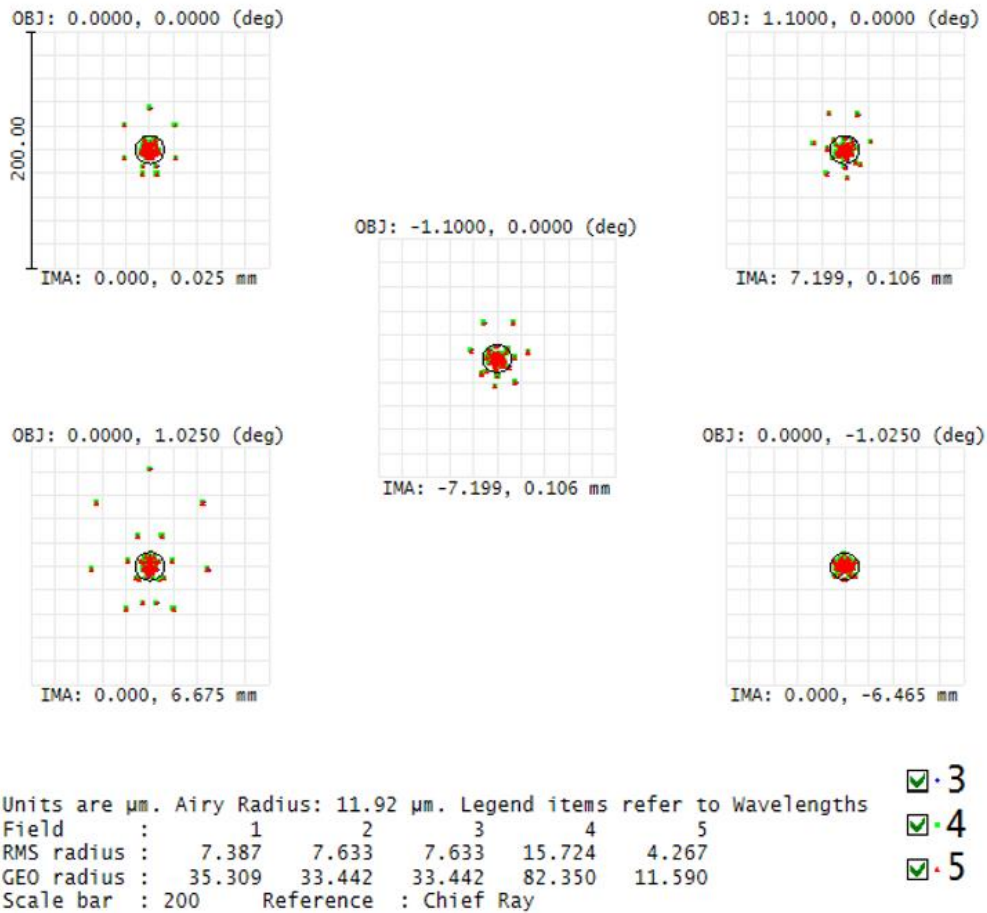ng et al. 2013). The tolerance parameters for this system analysis are defined in Kim et al. (2010). Despaces are defined as the inter-mirror distances, and in-plane movements are defined as x- and y-decenters (Park et al. 2020). Table 2 contains the parameters for the sensitivity analysis. These parameters apply to all the mirrors in the system. The sensitivity analysis conducted for this research was done using Ansys Zemax.

3.2.1 Monte-Carlo Simulation Parameters and Assumptions

The Monte-Carlo simulation is the most used method of conducting statistical analysis on system tolerances. It is effective at simulating comprehensive performance error with the errors all together at once. The results from this Monte-Carlo Simulation for sensitivity analysis are found in Figure 5. The Monte-Carlo Simulation computed the changes using the Root-Sum-Square (RSS) method.

Table 2: Monte-Carlo Simulation Parameters for OA-TMA

Parameter	Tolerance Range
Despace	±0.5 mm
Decenter	±0.15 mm
Tilt	$\pm0.02°$
Focus (Compensator)	±0.5 mm

The sensitivity analysis was performed on the tilt, decenter, and despace of each mirror. The sensitivity analysis results show that the most sensitive parameters for the system in order are the negative x-tilt of M3, the despace from M2 to M3, the y-tilt on M3, the decentration of

M3 in the negative y-direction, the x tilt of M1, the decentration of M2 in the positive y-direction, the positive x-tilt of M2, and the decentration of M3 in the negative x-direction. All other parameters are not significantly sensitive to their manufacturing errors.

The Monte-Carlo simulation consisted of ten thousand trials. The reference wavelength for this analysis was the primary wavelength in the system which is 4 µm. The two-pixel width of the camera selected for use in this system is 20 µm. This corresponds to a cumulative probability of approximately 98.6%. This indicates that the system is robust to manufacturing errors. All the tolerances, apart from the mirror tilts, are considered loose. It is commonplace to assemble and integrate optical systems achieving a centration ±0.1 mm translationally to the center of mirrors, so ±0.5mm is a larger margin (Park et al. 2020).
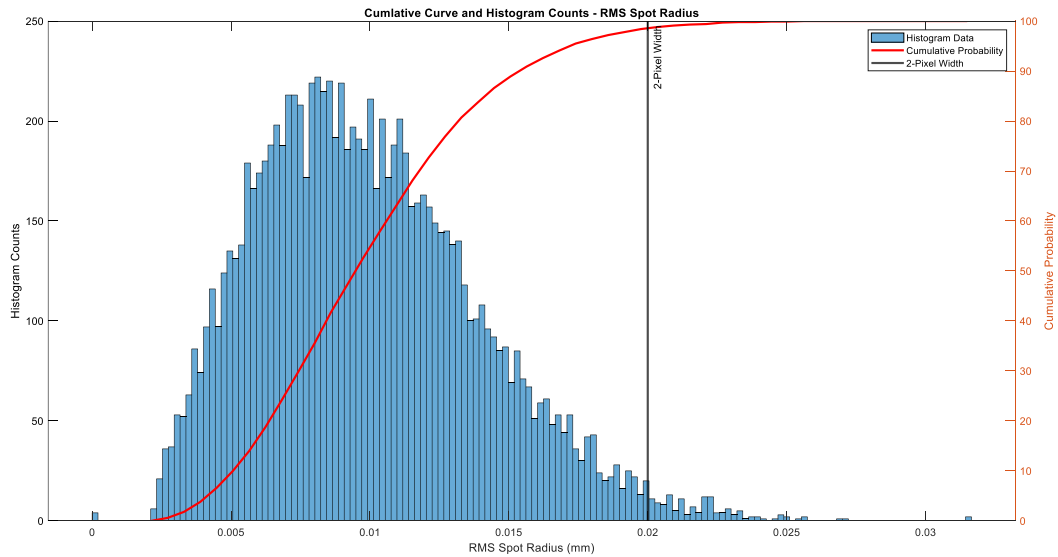
3.2.2 Monte-Carlo Simulation Results

Figure 5: Monte-Carlo Probability Diagram Including Nyquist Frequency.

In Figure 5, the cumulative distribution of the resulting wavefront spot diameter post sensitivity analysis. The 2-pixel width is indicated by the black vertical line. These results are from the Monte-Carlo simulation, and they confirm the performance of the optical system.

The depicted RMS spot radii in Figure 5 that resulted from the Monte-Carlo Simulation that exceeded the Nyquist sampling would be corrected in the assembly and integration process using adjustments in the mounting system. This adjustment capability is built-in to the optomechanical design. This will be further addressed in the optomechanical design section of this paper.

Table 3: Monte-Carlo Simulation OA-TMA Sensitivity Analysis Worst Offenders

Error Type	Mirror	Tolerance Value	Criterion	Change
x-tilt	3	-0.02°	0.01405036 mm	0.01357298 mm
Pos. Despace	2 to 3	0.5 mm	0.01065266 mm	0.01001461 mm
y-tilt	3	±0.02°	0.01063888 mm	0.00999995 mm
y-decenter	3	-0.15 mm	0.00938056 mm	0.00864917 mm
x-tilt	1	0.02°	0.00913531 mm	0.00838255 mm
x-tilt	3	0.02°	0.00875038 mm	0.00796130 mm
y-decenter	2	0.15 mm	0.00761299 mm	0.00669110 mm
x-tilt	2	0.02°	0.00714645 mm	0.00615508 mm
x-decenter	3	-0.15 mm	0.00666305 mm	0.00558654 mm

The strong performance of this system across all fields, even with the tolerances of ±0.5 mm despacing and focus compensation, ±0.15 mm centration, and 0.02° is due to the shape of the mirrors. The mirrors are freeform in shape. They will have the necessary thickness to be flat

on the back when manufactured to allow for easier optomechanical packaging of the system optics.

3.3 Freeform Mirror Design

The mirror surfaces were modeled in Ansys Zemax using the X-Y Polynomial surface type in sequential mode. The equation for the surface SAG for this surface type is shown in Equation (2) (Park et al. 2020).

$$z = \frac{\left(\frac{1}{R}\right)r^2}{1+\sqrt{1-(1+k)\left(\frac{r}{R}\right)^2}} + \Sigma_{j=2}^{66} C_j x^m y^n \qquad (2)$$

The coefficients for C_j that do not appear on Table 3 below are 0. This is due to symmetry about the Y-Z plane, or the x variables (Chang 2019). The term R in Equation (2) refers to the radius of curvature of the mirror. R refers to the radial pupil distance, so r^2 is $x^2 + y^2$. The k term in the above equation refers to the conic constant of the mirror surface. The resulting polynomial that specifies the surface shape can be found using Equation (3) (Park et al. 2020).

$$j = \frac{(m+n)^2+m+3n}{2} + 1 \qquad (3)$$

The resulting polynomial that is used to determine the shape of each mirror is Equation (4) below.

$$z = \frac{\left(\frac{1}{R}\right)r^2}{1+\sqrt{1-(1+k)\left(\frac{r}{R}\right)^2}} + C_4x^2y^0 + C_6x^0y^2 + C_8x^0y^3 + C_{10}x^2y^1 + C_{11}x^4y^0 + C_{13}x^2y^2 +$$

$$C_{15}x^0y^4 + C_{17}x^4y^1 + C_{19}x^2y^3 + C_{21}x^0y^5 + C_{22}x^6y^0 + C_{24}x^4y^2 + C_{26}x^2y^4 + C_{28}x^0y^6 +$$

$$C_{30}x^6y^1 + C_{32}x^4y^3 + C_{34}x^2y^5 + C_{36}x^0y^7 + C_{37}x^8y^0 + C_{39}x^6y^2 + C_{41}x^4y^4 + C_{43}x^2y^6 +$$

$$C_{45}x^0y^8 + C_{47}x^8y^1 + C_{49}x^6y^3 + C_{51}x^4y^5 + C_{53}x^2y^7 + C_{55}x^0y^9 + C_{56}x^{10}y^0 + C_{58}x^8y^2 +$$

$$C_{60}x^6y^4 + C_{62}x^4y^6 + C_{64}x^2y^8 + C_{66}x^0y^{10} \qquad (4)$$

Table 4: Mirror Shape Parameters for Freeform Mirrors of the OA-TMA

Parameter	M1	M2	M3
1/R	-6.87E-04 mm^{-1}	-2.88E-03 mm^{-1}	-2.02E-03 mm^{-1}
k	-4.88E-01	4.26E-01	2.66E-01
C_4	1.58E-01	4.31E-01	-1.28E-01
C_6	-3.11E-01	1.05E+00	4.21E-01
C_8	-3.93E-02	7.54E-01	2.13E-01
C_{10}	-1.88E-02	4.07E-01	1.50E-02
C_{11}	7.81E-02	-3.90E-02	1.37E-02
C_{13}	-1.49E-02	1.87E-01	6.41E-02
C_{15}	-5.63E-03	-1.07E-01	-1.11E-02
C_{17}	-6.76E-02	1.68E-01	3.82E-02
C_{19}	2.72E-03	-2.09E-02	3.13E-02
C_{21}	2.34E-04	7.07E-02	-1.39E-03
C_{22}	1.95E-01	3.10E-02	-3.11E-03
C_{24}	1.80E-02	-2.45E-01	2.85E-02
C_{26}	3.60E-04	2.33E-01	4.29E-03
C_{28}	1.59E-04	-5.62E-02	1.45E-03
C_{30}	-4.49E-02	-4.61E-02	-2.53E-03
C_{32}	-2.98E-04	3.82E-01	-1.11E-03
C_{34}	4.57E-06	-2.32E-01	-2.95E-03
C_{36}	-2.11E-05	-2.32E-01	2.65E-04
C_{37}	-2.14E-01	-2.19E-01	3.10E-03
C_{39}	-1.41E-02	5.18E-01	3.95E-04
C_{41}	-3.29E-04	-3.07E+00	-1.47E-02
C_{43}	-1.27E-05	1.16E+00	-2.15E-03
C_{45}	7.60E-07	-4.98E-02	-3.21E-04
C_{47}	9.26E-02	2.17E-01	2.98E-03
C_{49}	4.46E-03	-9.53E-01	1.06E-03
C_{51}	8.20E-06	-7.54E-01	-7.49E-03
C_{53}	3.15E-06	2.04E+00	-5.53E-04
C_{55}	5.47E-09	-1.72E-01	-1.42E-04
C_{56}	2.65E-04	5.30E-01	-1.93E-04
C_{58}	-1.00E-02	-3.55E+00	8.02E-04
C_{60}	-2.81E-04	1.49E+01	2.41E-04
C_{62}	2.66E-06	-6.47E+00	-1.22E-03
C_{64}	-2.82E-07	-4.49E-01	-5.86E-05
C_{66}	2.43E-09	5.12E-02	-1.95E-05

The coefficients shown resulted from the optimization process. They were set as variables in the optical model for this optimization. This allowed for high performance, and this decision was made because manufacturing costs are not a factor for this study.

3.4 Through-Focus Spot Diagram

An analysis of the through-focus spot size was conducted on this system. For reference, the Airy disk radius for the primary wavelength in the system is 11.92 µm. This technique describes the performance of the system through a range of focus. The range of defocus in this analysis is 300 µm. At the extrema of the analysis, the spot size is roughly 3 times larger than the diffraction limit which demonstrates an overall sensitivity to defocus. The speed of the system is responsible for the short depth of focus. Figure 6 shows the visual representation of the spot behavior as the system is defocused. The result is a tight tolerance where the acceptable level of

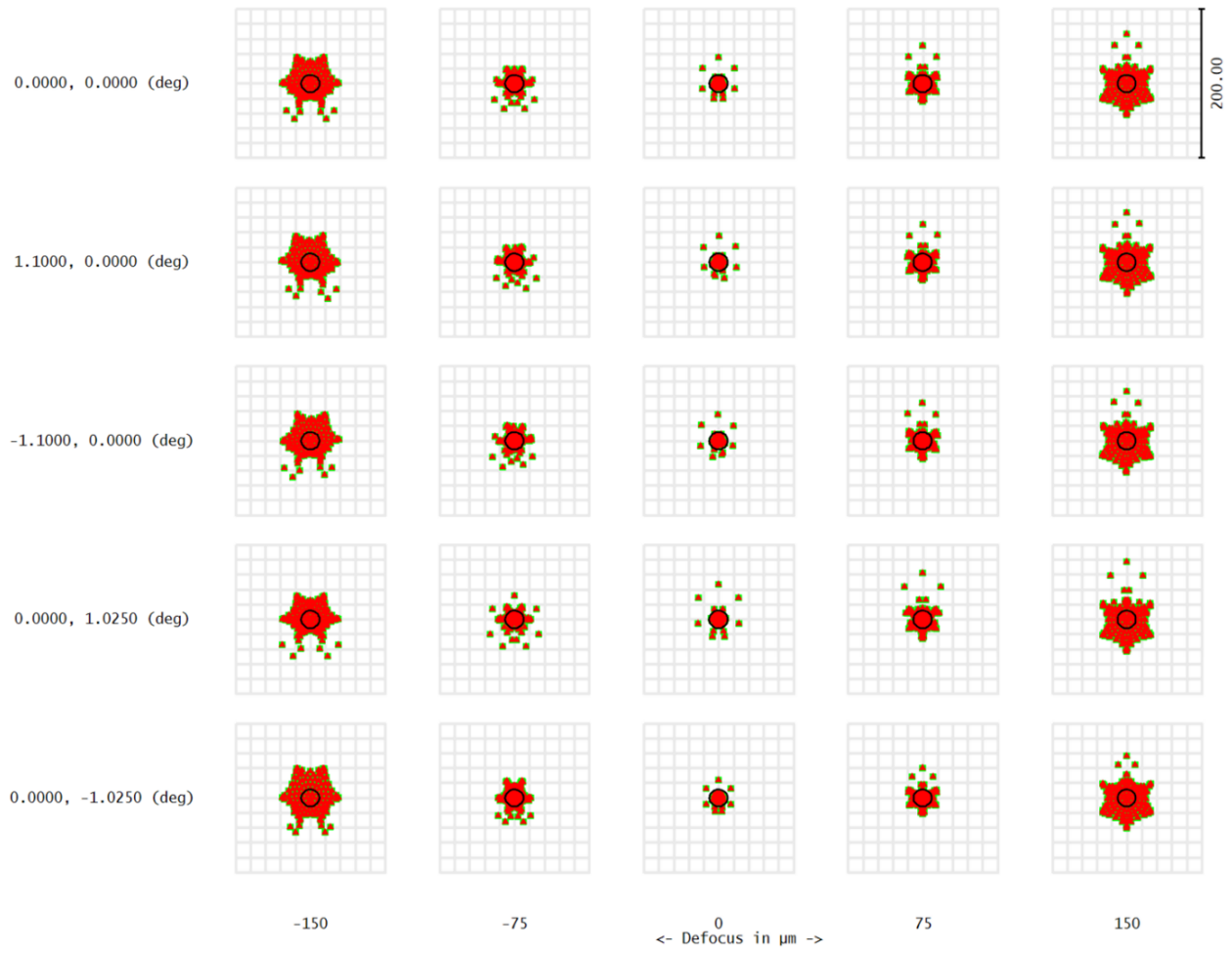defocus is ±100, the results for which are shown in figure 7.

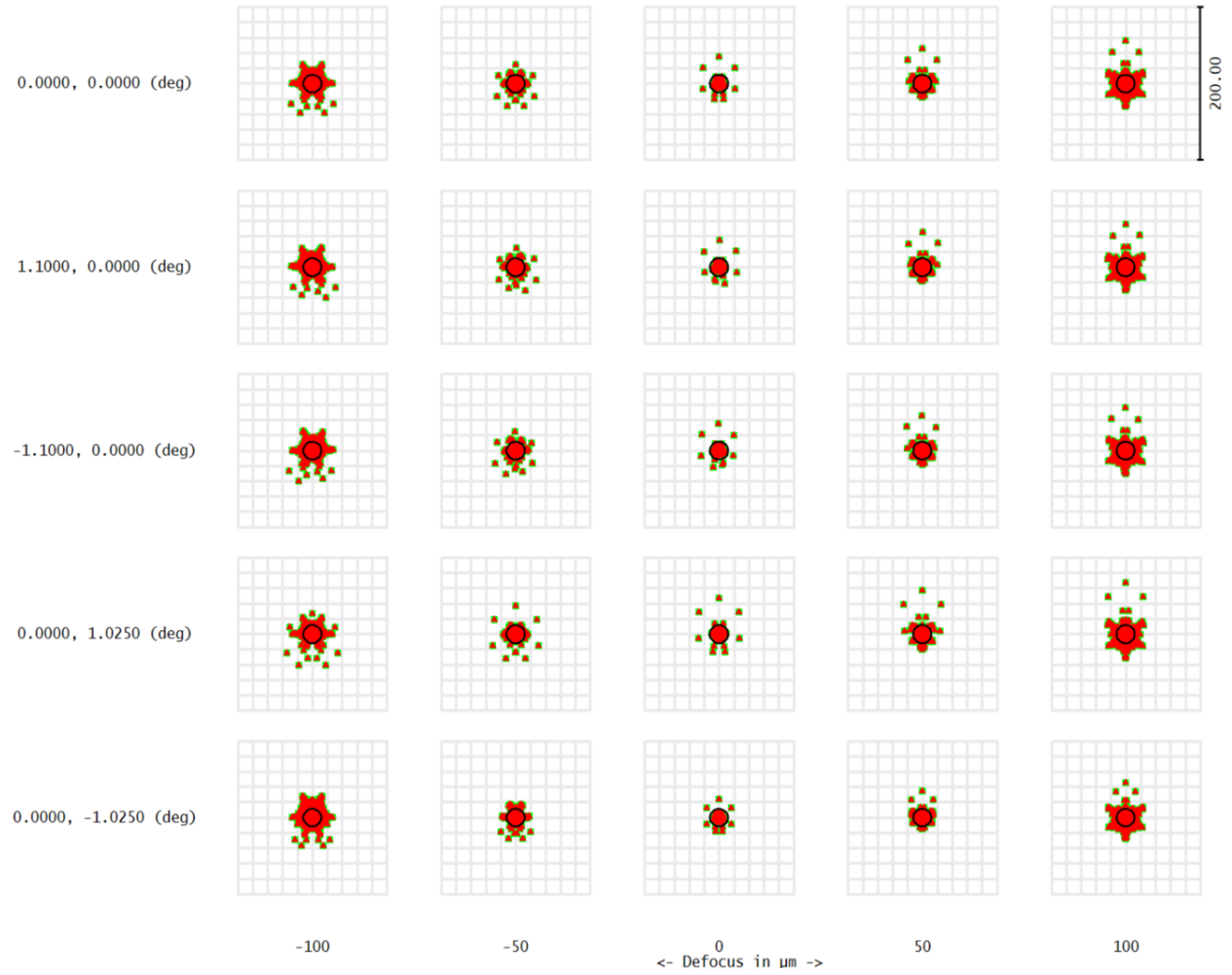**Figure 6: Through-focus Spot Defocused OA-TMA**

Figure 7: Acceptable through-focus spot diagram

The anomaly of the spots' shapes in Figure 7 comes as a result of the freeform shape of the mirrors. Figure 8 shows the shape of the mirrors with exaggerated diameters to lend insight into the effect in Figure 7.
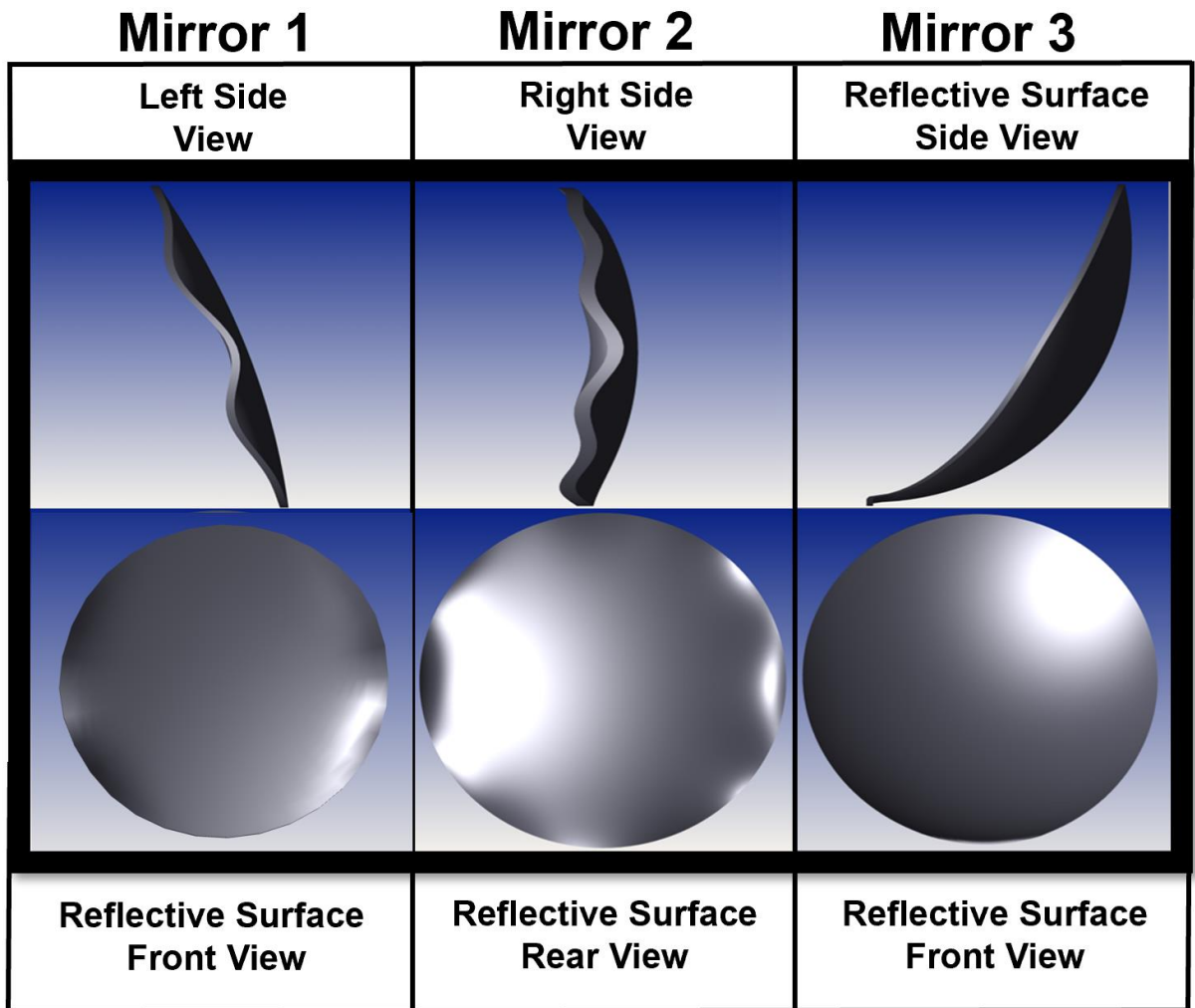
Mirror 1	Mirror 2	Mirror 3
Left Side View	Right Side View	Reflective Surface Side View
Reflective Surface Front View	Reflective Surface Rear View	Reflective Surface Front View

Figure 8: Augmented Diameter Mirrors

Although all three mirrors contribute to the anomaly shown in Figure 7, M2 has the most significant effect on the shape of the spots.

3.5 Optical Path Difference

The optical path difference (OPD) aberration analysis measures the difference between the optical path length of real rays and the ideal chief rays. That difference is commonly known as optical aberrations. The OPD across four of the 5 fields is less than ±0.25 waves, which means that the aberrations for those four fields are insignificant (Fischer et al. 2008). The fifth field is

still less than ±0.5 waves, so while the aberrations will have more of an impact on the

performance, the aberrations still have little effect. Figure 9 shows the OPD plots for this system.
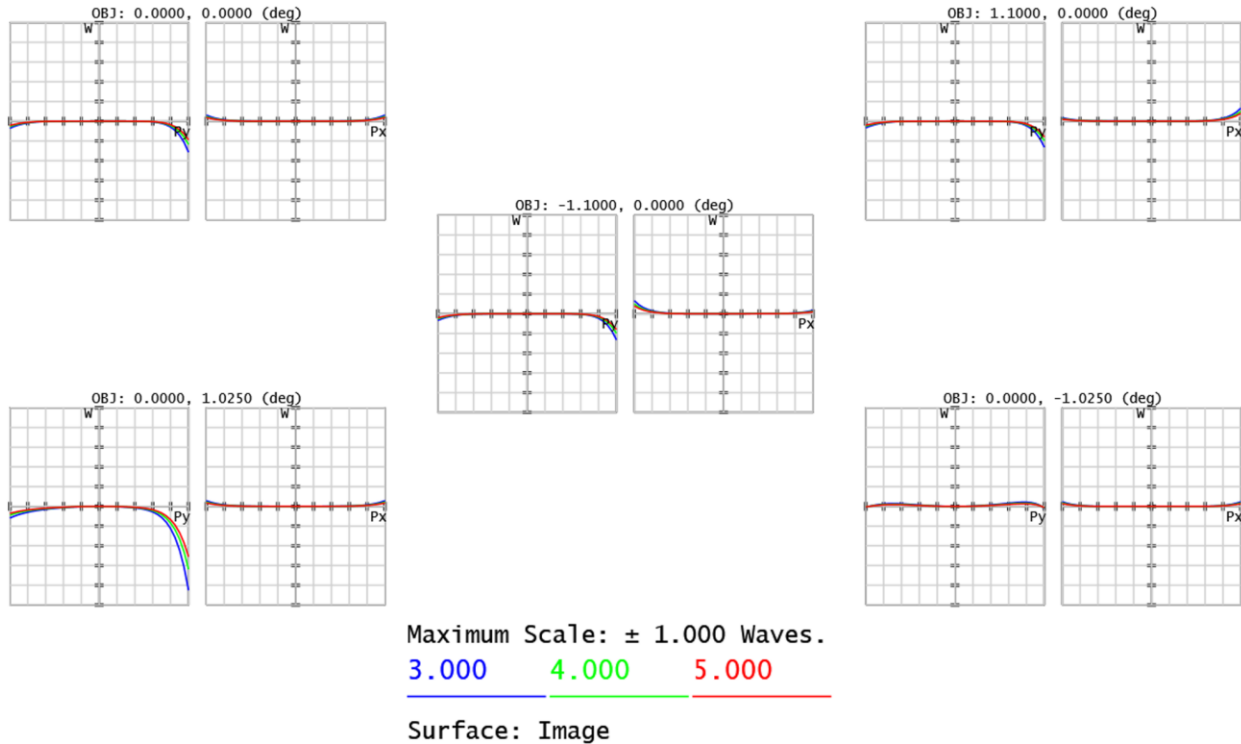

Figure 9: Optical path difference aberration plot

3.6 Field Curvature and Distortion Performance

Field Curvature is an aberration that describes the curvature of the image plane. If field

curvature exists in a system, the image points are projected not onto a paraxial image plane, but a

curved image plane. There are some situations where the field curvature is biased in one

direction, and the way that field curvature can be corrected is by rotating the image plane to

offset the curvature. Figure 10 shows the field curvature and distortion plots. Due to the angular

sensitivity of the system, the maximum distortion is 1.2805% and the maximum field curvature is 0.9 µm sagittal and 11.5 µm tangential. The tangential aberration is greater than the sagittal aberration. The results obtained from this analysis are similar to those determined from the OPD analysis. This is another confirmation of the system's performance.
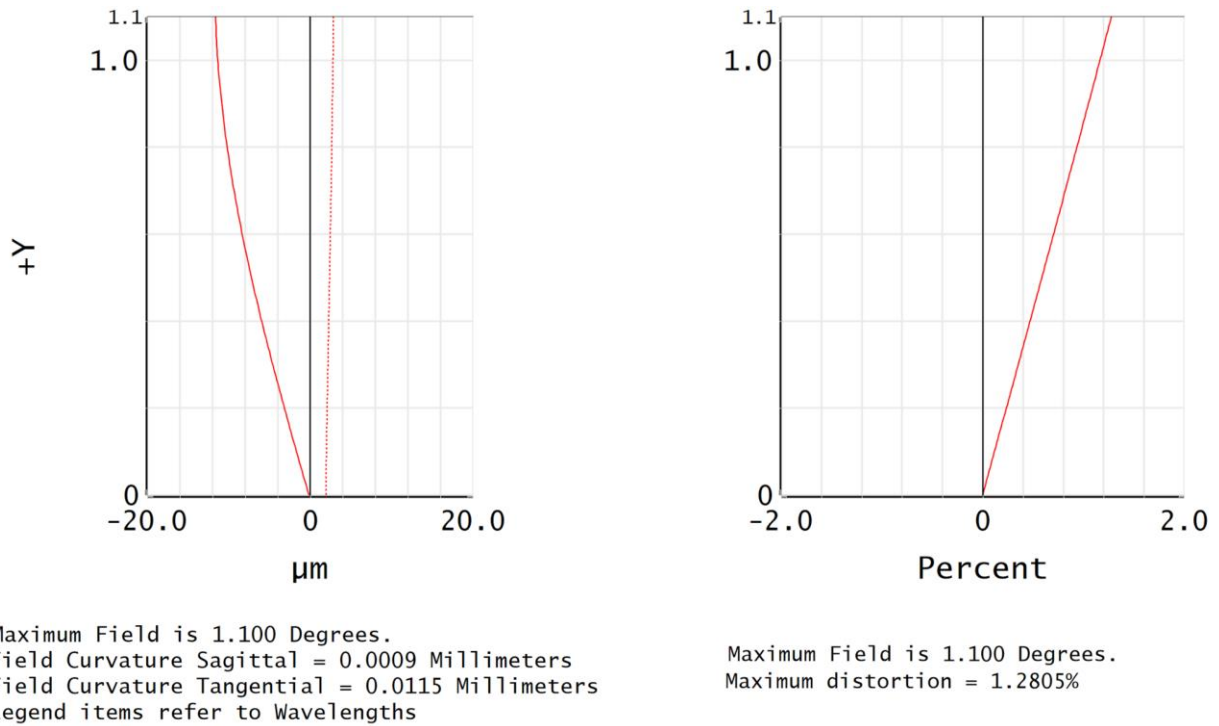

Maximum Field is 1.100 Degrees.
Field Curvature Sagittal = 0.0009 Millimeters
Field Curvature Tangential = 0.0115 Millimeters
Legend items refer to Wavelengths

Maximum Field is 1.100 Degrees.
Maximum distortion = 1.2805%

Figure 10: Field curvature and distortion performance plot

3.7 Seidel Coefficients Analysis

The Seidel Coefficients are a measure of wavefront error in an optical system. They describe how well corrected the system is for aberrations. Figure 11 shows the plot of the Seidel coefficients. The system is dominated by spherical aberration; the coefficient for the total spherical aberration in the system is about 0.15 mm. M3 is responsible for most of the spherical aberration in the system. M2 follows, but its coefficient has the opposite sign of the spherical

31

aberration coefficient for M3. This helps reduce the total spherical aberration in the system. The magnitude of the spherical aberration coefficient for M1 is far less than that of the other two mirrors.
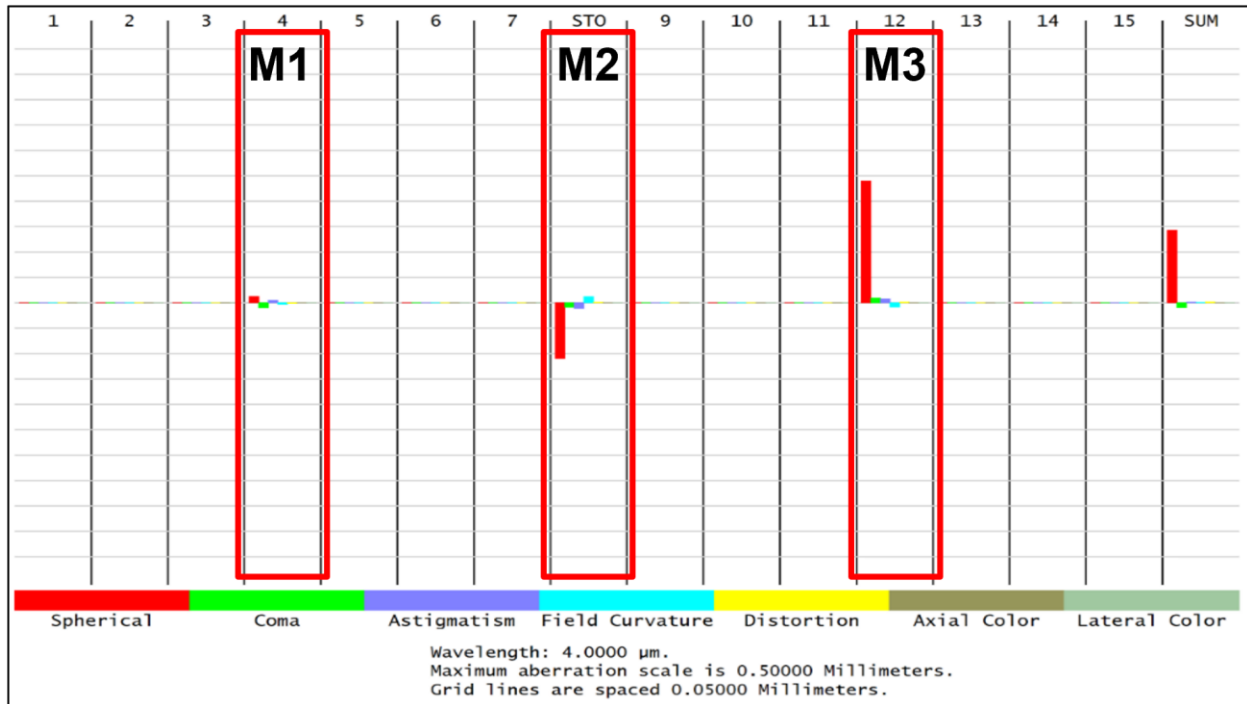

Figure 11: Siedel coefficients analysis plot. Surface 4 is M1, the STOP is M2, and surface 12 is M3.

3.8 Point Spread Function Analysis

The point spread function (PSF) describes the physical performance of an optical system. The PSF specifically simulates imaging a point source to determine the resolution of the OA-TMA. The PSF is mathematically described the object's diffraction through an optical system. The ideal object is modeled using a two-dimensional delta function. This can be thought of as a large on-axis intensity and near zero off-axis intensity. This function considers all the aberrations in the system that result in the formation of image blur (Greivenkamp 2004).

32

The Strehl Ratio (SR) describes the optical performance of an optical system. It quantifies the resolution of an optical system. The higher the SR is, the better the optical system performs. The way the SR is calculated is by dividing the peak diffraction pattern intensity by the maximum intensity for an ideal system. Optical systems are considered diffraction limited when the SR is greater than or equal to 0.8 (Guenther et al. 2018). This indicates that the system can resolve its physical resolution limit. Near 1 SR produces a diffraction pattern with almost all the power concentrated in the center. The further from 1 the SR is, the more spread out the diffraction pattern is. It is always best practice to design a system to produce the highest SR possible with the components for use in a design. Figure 12 shows the PSF for this system. The SR across all fields is above 0.8. This indicates high performance in the optical system across all fields.
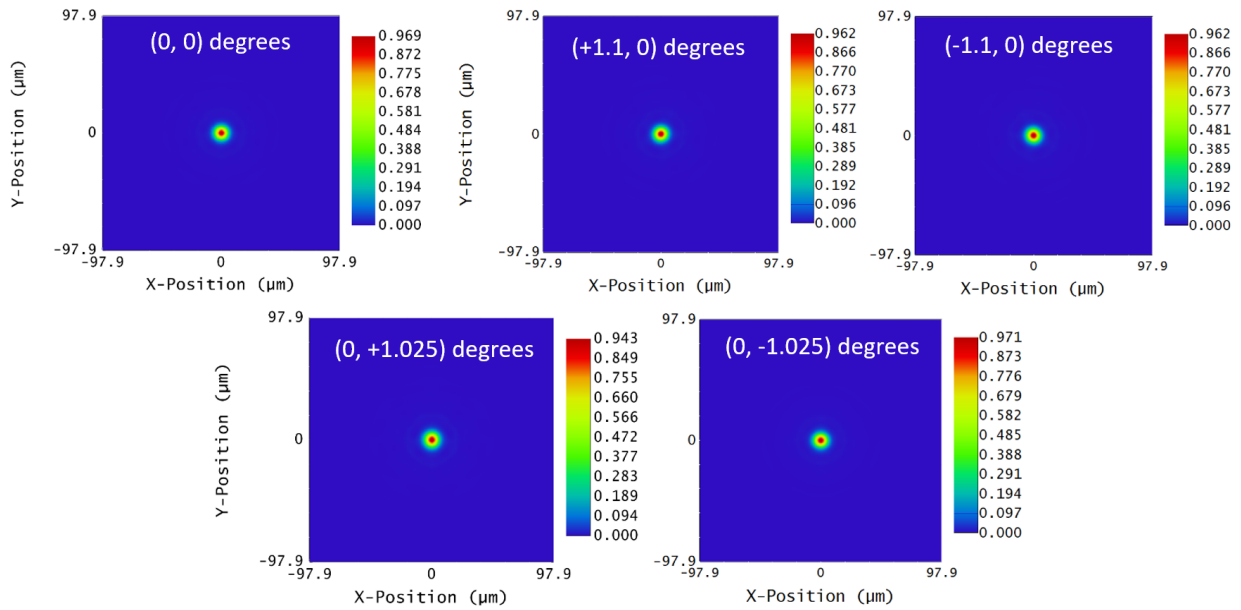

Figure 12: Point spread function analysis plot.

3.9 Longitudinal Aberration Analysis

Longitudinal aberration is the deterioration of the performance of an optical system that happens when the image plane is not aligned with the marginal tangential rays along the optical axis. Longitudinal aberration will cause image blur and a reduction in contrast in an optical system. The longitudinal aberration in this system, the plot for which is shown in Figure 13, shows highly degraded performance starting at about 90% of the EPD coordinate. The y-axis of the plot shows the normalized EPD, and the x-axis shows the aberration as a function of the normalized pupil height (Fischer et al. 2008).
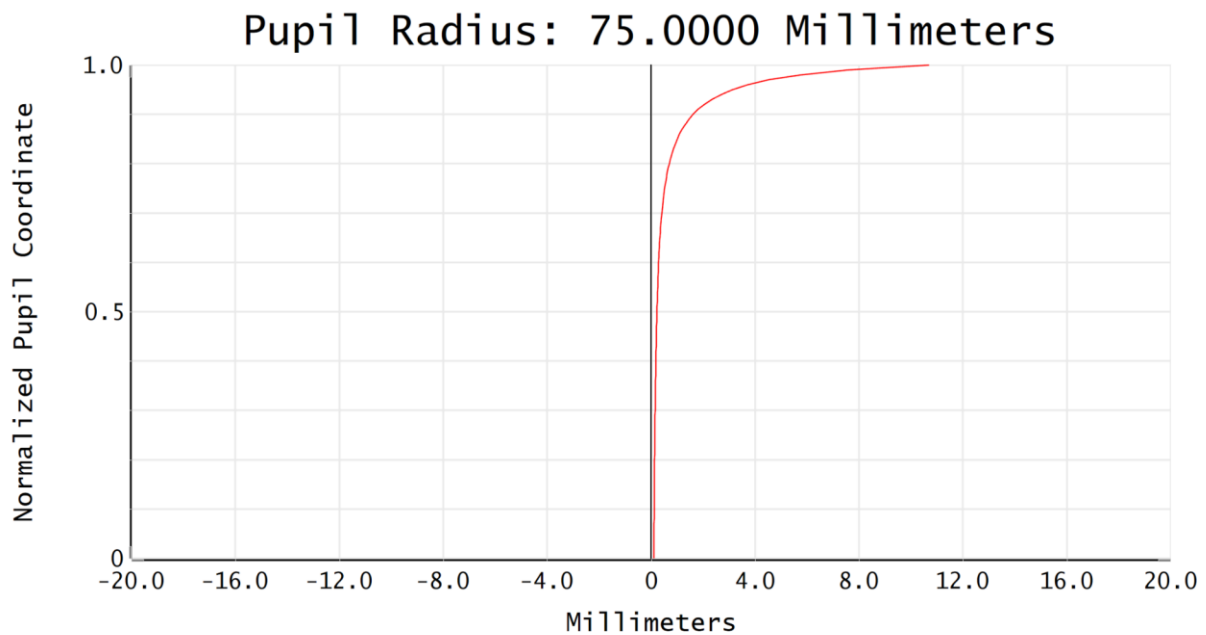
Figure 13: Plot showing the longitudinal aberration in the system.

3.10 Modulation Transfer Function (MTF)

The modulation transfer function (MTF) is a parameter that describes the spatial frequency-dependent performance of a system. The MTF simply shows how well a system reproduces the contrast in the image. MTF is a function of spatial frequency in units of cycles/mm. The Nyquist frequency is the maximum frequency at which a system can sample which correctly reproduces the original signal without aliasing (Fischer et al. 2008). The Nyquist frequency of the system is the inverse of twice the Airy disk diameter (Fisher et al. 2008). For this system, the Nyquist frequency is 41.9463 cycles/mm. The MTF is above 0.4 for all fields at the Nyquist frequency. This indicates performance that is adequate for the desired application.
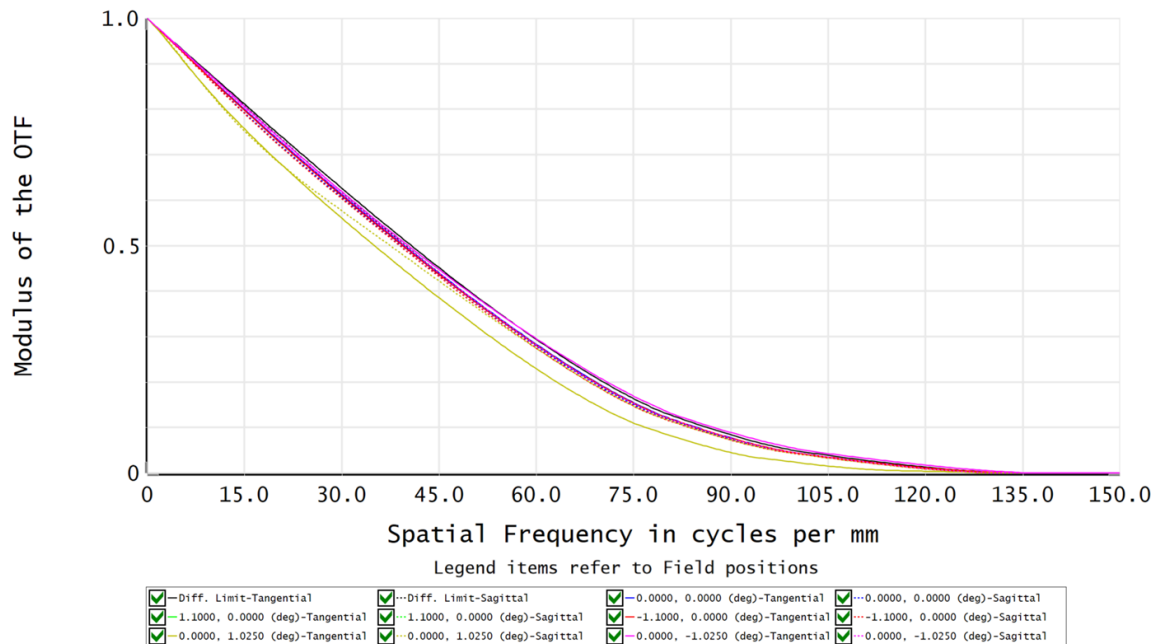

Figure 14: Plot of the Modulation Transfer Function

3.11 Encircled Energy Plot

Another metric on which to gauge the performance of an optical system is encircled

energy. It is a fraction of the total optical power. It characterizes how well a system focuses light

into a single spot onto the image plane. A strong and commonly used requirement for energy

encircled from a point source in the Airy disk radius (Fischer et al. 2008). According to the

analysis, the enclosed energy at the Airy disk radius is about 84% indicating diffraction limited

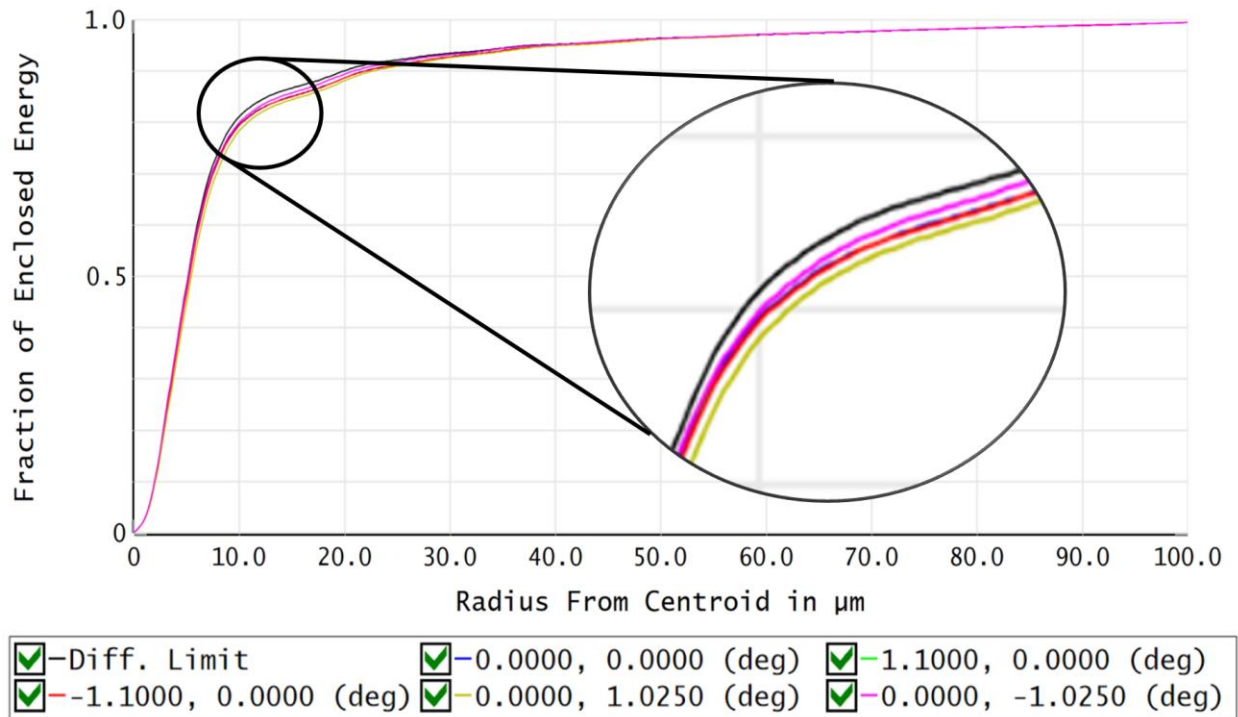performance. This allows for the parameters in Table 2 for the optical tolerancing.

Figure 15: Plot of the Encircle Energy

4. Opto-Mechanical Design

The opto-mechanical design is the novelty in this system. The terms that will be used to describe the status of the optical system will be "stowed" when the telescope is folded into its transportation configuration, "deployed" when the system has arrived at its destination and has completed its unfolding task, and "deployment-in-progress" when the telescope system is switching between those two configurations. The purpose of this section is to describe the goals and methods used to achieve those goals for inventing a method of stowing and deploying an OA-TMA and how it can deploy. All other analyses are out of the scope of this project.

Once the system has successfully unfolded, it will remain deployed. The mirror mounts have 5 degrees of freedom for adjustment. Those adjustments are x- and y-translation, tip, tilt, and roll. These adjustment capabilities allow the system to be realigned when necessary. The despacing, once set, is not adjustable. This parameter would be solidified during the integration and testing process of the system.

The optomechanical design is broken up into 4 major subassemblies: Primary Mirror Assembly (PMA), Secondary Mirror Assembly (SMA), Tertiary Mirror Assembly (3MA), and Camera Assembly (CA). The SMA is the only major subassembly that does not move during deployment. The deployment process is discussed in greater detail in section 4.1.2. Figure 16 below shows each subassembly. Isometric and front views are used for displaying the assemblies.
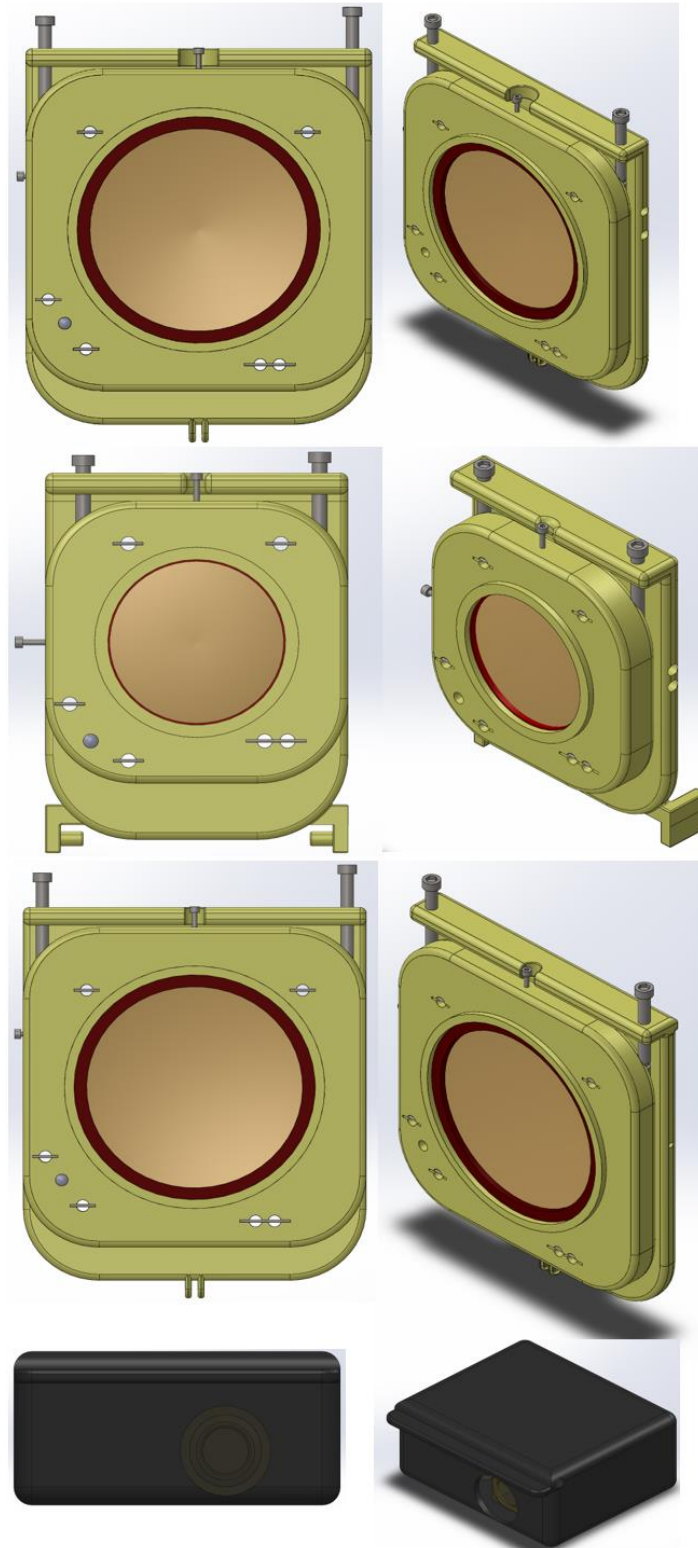
Figure 16: Primary, Secondary, and Tertiary Mirror Assemblies

4.1 TMA Material Choices

The materials used for the optomechanical packaging for this system is Invar 36. The purpose of using Invar 36 for all metallic materials is for the low thermal coefficient of expansion and hardness. This makes the material excellent for space use as there are wide temperature ranges that a space observatory experiences. The hardness of the material assists the system in maintaining its shape. The system's ability to maintain its shape is critical to the survivability and preservation of its performance though a deployment. The substrate onto which the mirror coating is applied is beryllium, much like the JWST (Park et al. 2020).

4.1.1 TMA Storability

The OA-TMA is stored in the manner shown in Figure 17. There are a total of eight folding arms that have tabs built into them which accept a lockout pin at full lockout. There is also an area contact at the specific complementary angle required for the primary and tertiary mirrors to achieve their required angles of incidents for nominal operation. The mounts for the primary and tertiary mirrors are also wider than that of the secondary which allows the tip and tilt adjustment screw to locate to the side of the secondary mirror mount without interference. The translation adjustments also do not interfere with the extension arms. The bottom of those same mirror mounts each have loops on them that join with the middle plate onto which all the optical assemblies of the mirrors are mounted. The Teledyne FLIR Neutrino QX is in the CA at the appropriate angle of incidence to match the Ansys Zemax model. The CA rotates back onto the back of the SMA. The stowed configuration is shown in Figure 17. All the joints that appear in Figure 17 are held together by an axle that fits in the holes.
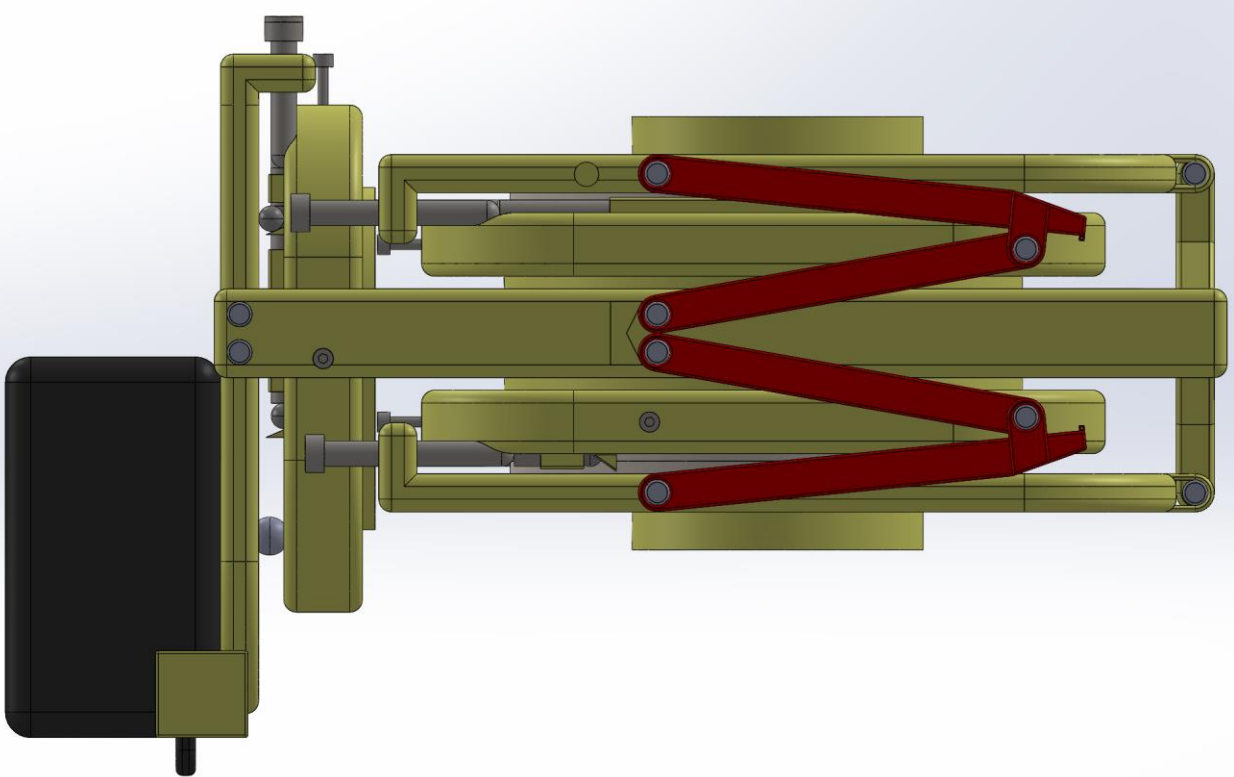
Figure 17: Stowed telescope configuration.

The stored OA-TMA fits inside a box of dimensions 295.00 mm x 299.27 mm x 482.55 mm. in comparison, the dimension of the box required to fit the OA-TMA when it is deployed is 295.00 mm x 793.03 mm x 547.50 mm. A figure showing the comparison between the volumes of the stowed vs deployed configurations is shown below. As shown in Figure 18, the stowed configuration has about 66.7% less volume per cubic unit volume than the deployed configuration. This system's footprint minimization aids in loading the system onto its launch vehicle and sending it into space.
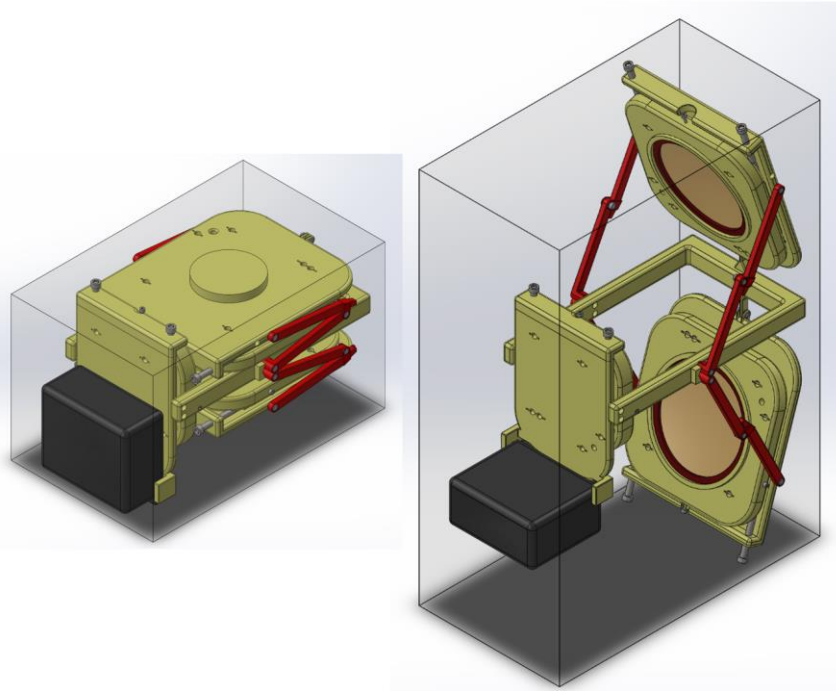
Figure 18: Stowed (right) and deployed (left) OA-TMA configurations.

The middle section is easily seen in the deployed configuration in figure 18 above. Great care was taken to avoid vignetting. The middle section has a rigid arm at the furthest portion from the SMA as assembled. This rigid arm is stationary. This means that there are fewer moving parts in the system. This keeps the design simpler with fewer components to malfunction. It also reduces the cost to manufacture, integrate, and test the system.

4.1.2 TMA Deployment

The telescope system deploys in a series of steps. The first is the unfolding of the primary mirror. The extension arm will unfold slowly to help prevent jitter caused by sudden movements. The range of travel for the extension arm is limited by an area of contact on the middle section component. There is also a small spring pin mechanism that activates when the extension arm is

at the limit of its travel. The two arms are locked in their full extension when the protruding feature on the first extension arm depresses a spring pin that is responsible for retaining the locking spring pin. Once the locking spring pin has deployed, the system will be locked out. The unfolding process for this mirror takes 2 days to execute.
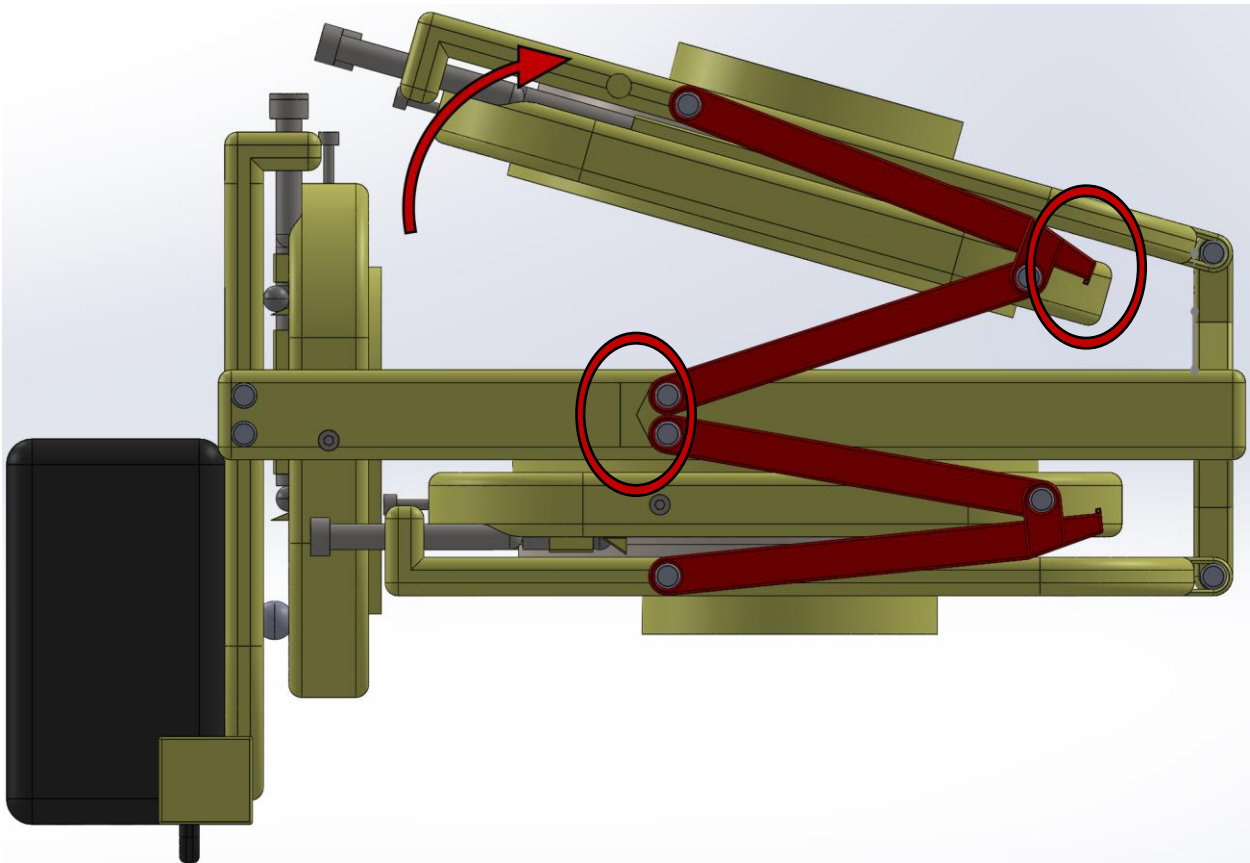

Figure 19: First step in OA-TMA deployment.

The second step is the same as the first step, but it is the 3MA that moves instead of the PMA. This process takes 2 days to execute. The extension arms that are used to deploy this branch have the same mechanism that the deployment system for the PMA had: a locking spring pin to lock the system out after it is deployed. The deployment of the mirrors happens one mirror at a time in the same way that the JWST deploys each primary wing individually.
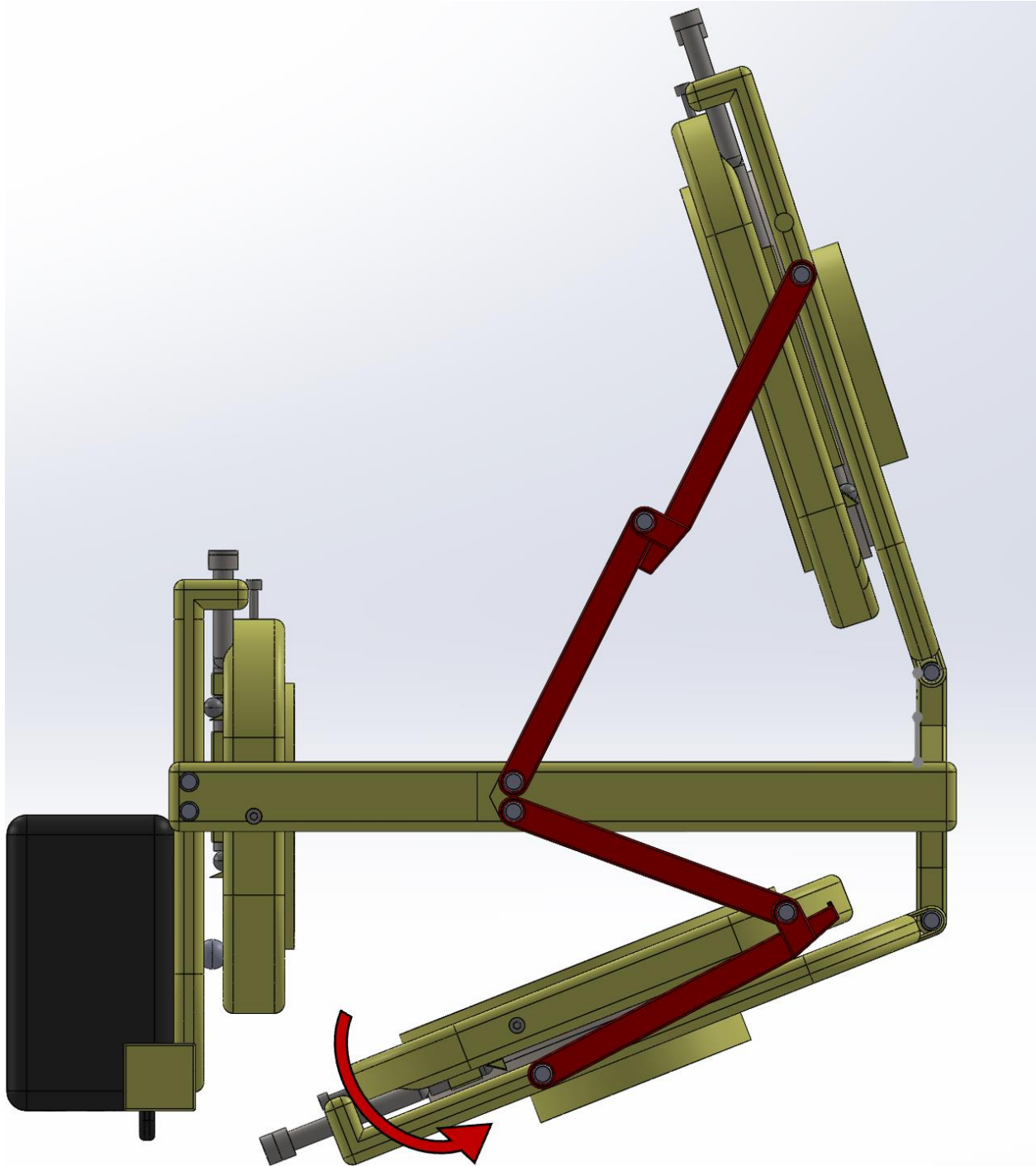
Figure 20: Second step in OA-TMA deployment

The third step in the deployment process is the unfolding of the CA. The CA unfolds and

has a ridge that acts as an area contact to stop the rotation, and captured spring pins deploy to act

as opposing line contacts to keep the CA from bounding back. This deployment process takes 2 days to execute.
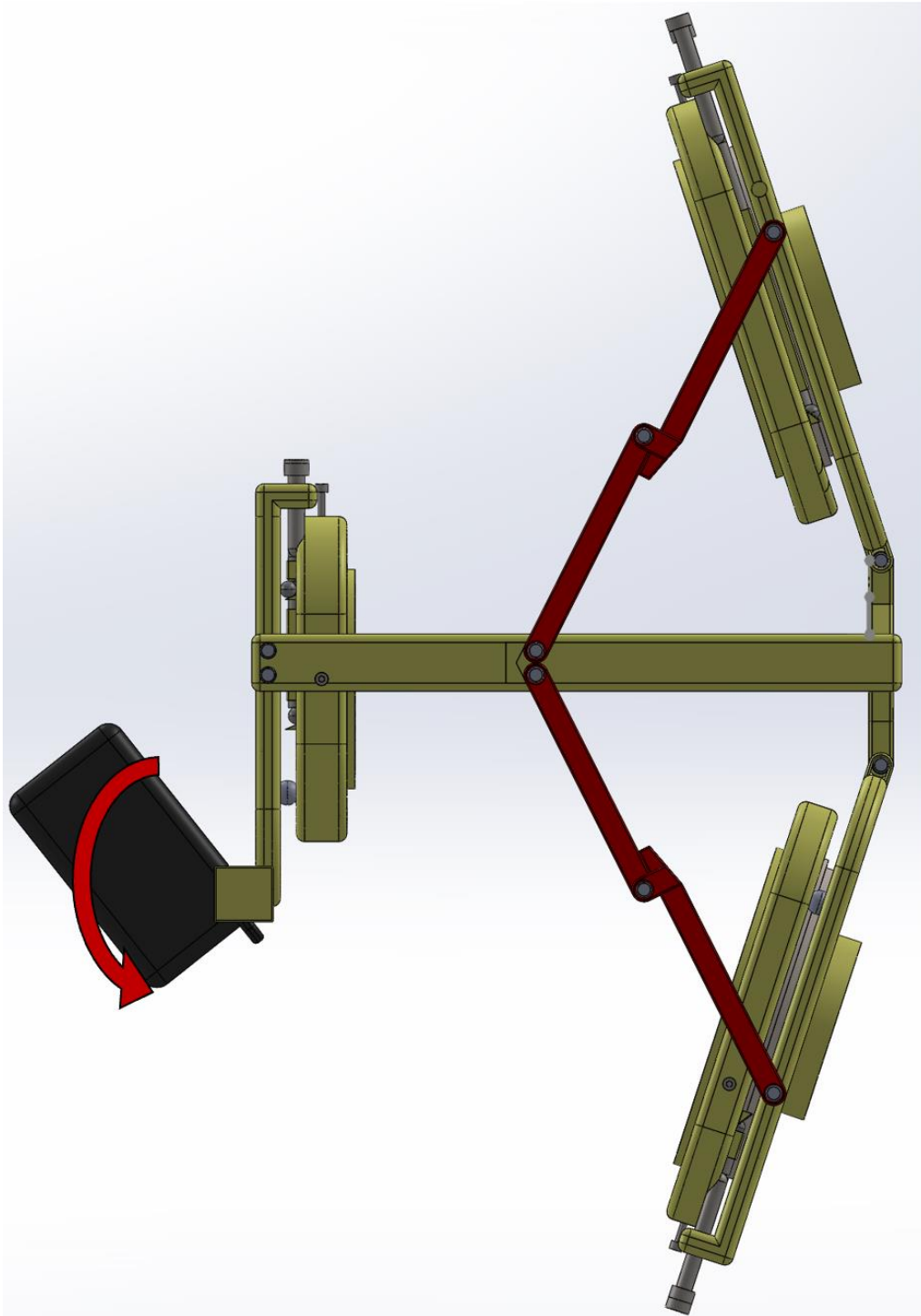

Figure 21: Third step in OA-TMA process.

The system in full deployment is depicted in figure 22. There are no interferences that prohibit the system from unfolding. However, the mechanisms mentioned earlier prevent the telescope from going back into its stored configuration. To protect the CA, a shutter is used to cover the detector when it is not in use. This will prolong the life of the system and help the system maintain the highest level of performance possible.
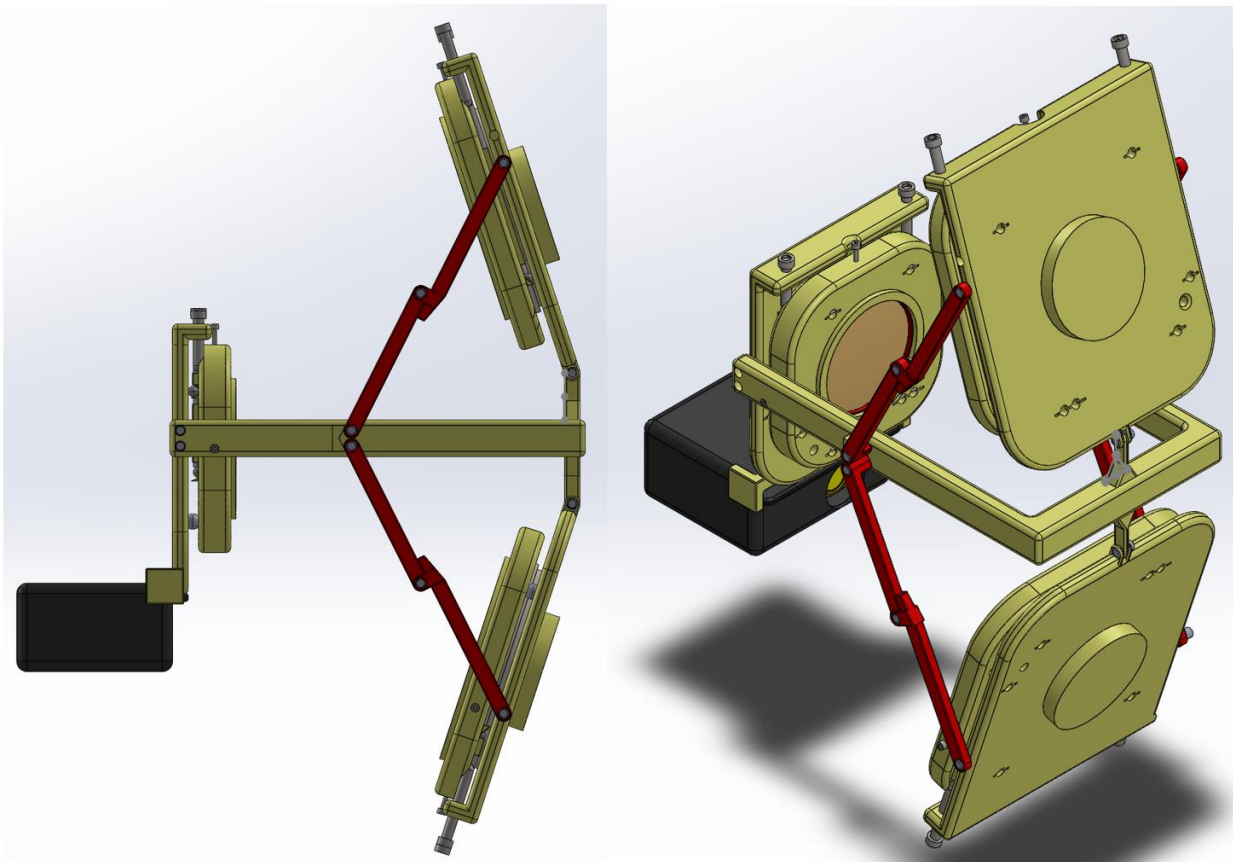
Figure 22: Full deployment configuration for the OA-TMA

4.2 Mirror Adjustment

Each mirror mount has 5 degrees of freedom: z-translation, y-translation, tip, tilt, and roll. Figure 23 provides a visual representation of these degrees of freedom. The adjustments

are made possible with precision machined mechanical components. They are precision
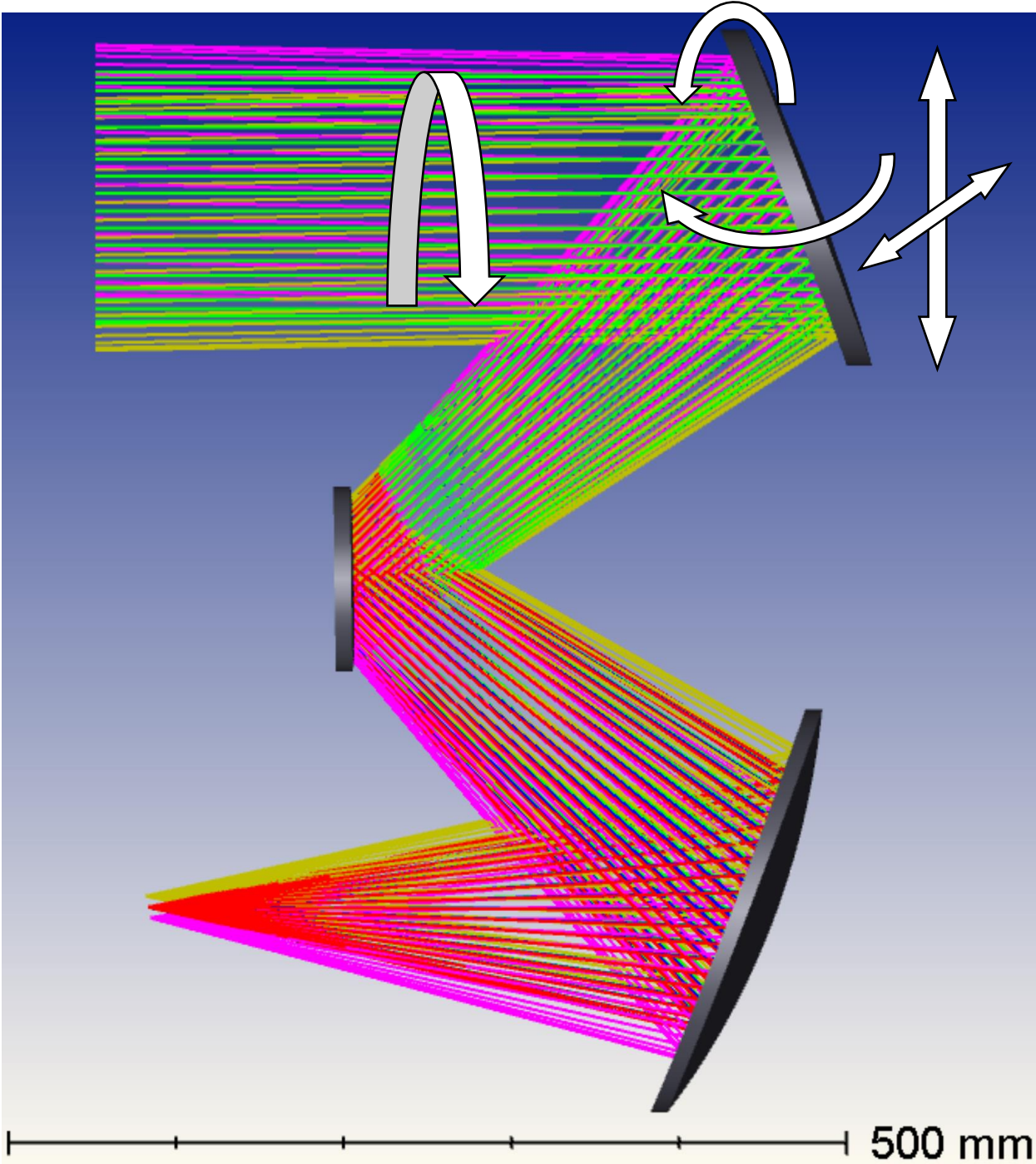
machined to allow for fine adjustments.

Figure 23: Mirror Adjustments for OA-TMA

The translation adjustments are achieved using the mirror cell, a fine-thread screws, and a spring-loaded block which provides an area of contact concentric with the mirror cell. The spring applies a force opposite that of the normal force applied to the mirror cell by the fine-threaded screw. This keeps the mirror cell in a state of constant contact with the mechanical components that keep it housed and allow for adjustments. This mechanism is applied in both the x- and y-axes. The mechanism is shown in Figure 24.
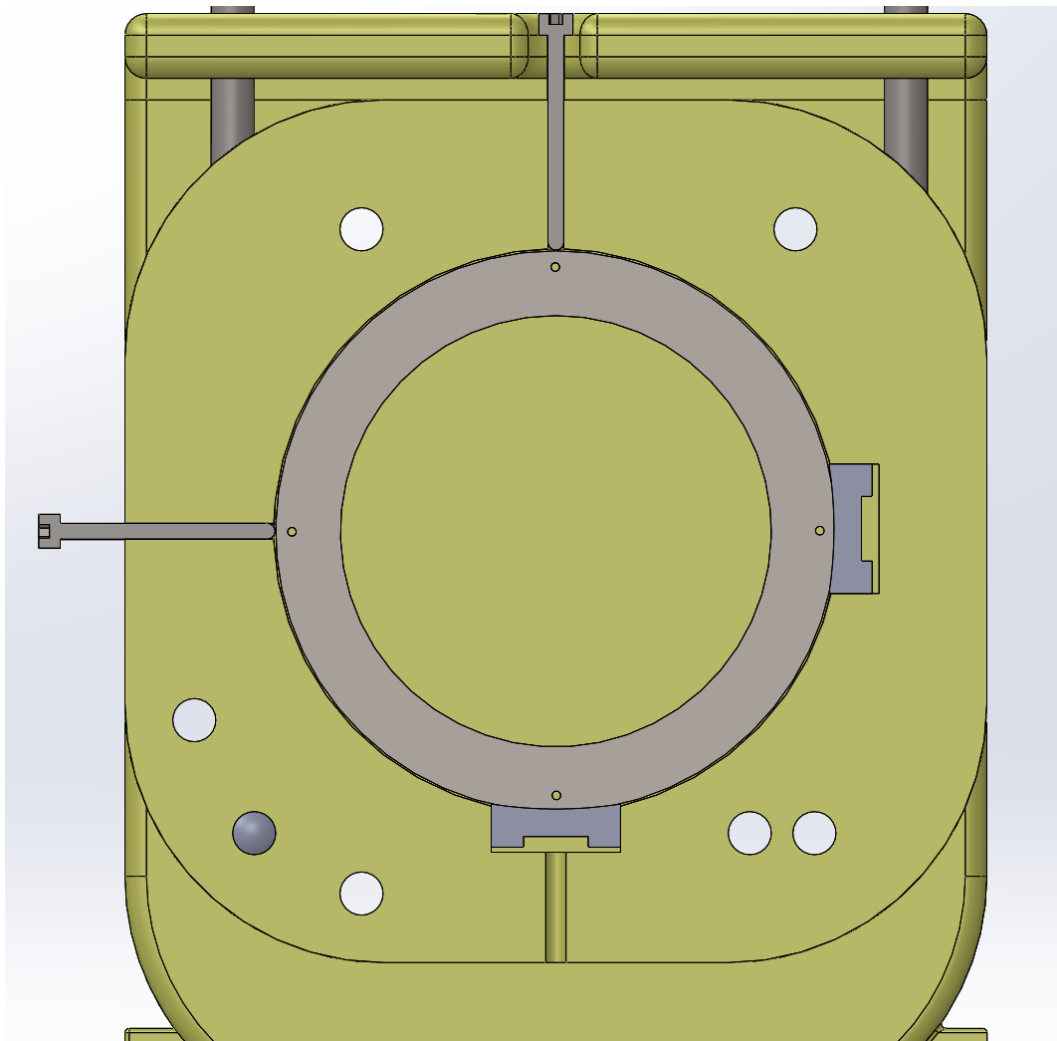

Figure 24: Translation adjustment kinematic system.

The tip and tilt adjustments are achieved using fine-thread screws, a sphere, a ramp, springs, pins, and a plate. The sphere provides a point contact between the ramp and the plate, and another with the pin that pushes the sphere up and down the ramp. The ramp pushes the sphere into the plate, and the springs pull the plate back into the sphere. The sphere is held in place by the plate, the ramp, and the pin. The physical mechanism is shown in Figure 25.
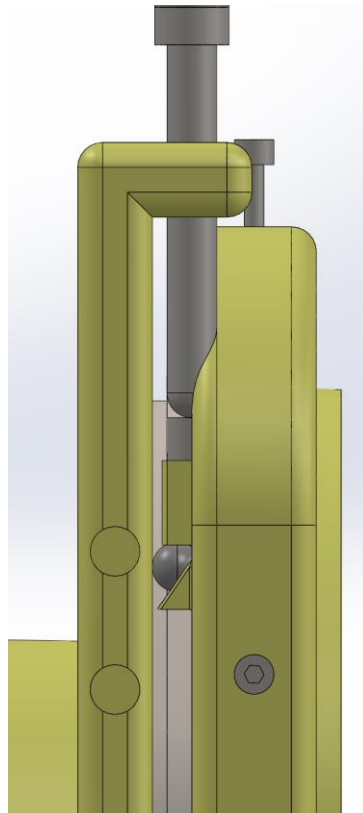
Figure 25: Tip and tilt kinematic adjustment systems.

The roll adjustment is executed by rolling the mirror cell. The mirror is held in place with set screws that are steaked with a high strength epoxy. The cell is not locked down by anything. This allows for roll adjustment if this level of adjustment is needed. Overall, the system can be packaged for space deployment as proven by the design. The adjustments are kinematic and precise. This system can therefore be aligned to perform within the diffraction limit.

5. Conclusion

The proposed OA-TMA is an ideal candidate for the next generation of space observatories. It is possible to get diffraction-limited performance across a wide FOV while avoiding the chromatic effects of refraction while also maintaining the wavelength indolence of an all-reflective system. The strong performance of the system was proven through thorough analysis.

The RMS spot radius is between 4.2670 µm and 15.724 µm. The Airy disk radius for the system is 11.92 µm, so the system performs at or below the diffraction limit across all fields. When the system is used with the FLIR Teledyne Neutrino QX, the system cumulative probability of a spot size being produced at or below the Nyquist frequency was 98.6%. The remainder of the analysis. This was the result of sensitivity analysis using realistic tolerance values.

This design proves the system is possible to package into a configuration suitable for space deployment. The stowed configuration is roughly 66.7% smaller than the deployed configuration. The stowed configuration's symmetry also makes it easier to load into a launch vehicle. Future steps for this project include finite element analysis of the system in its stored configuration, selection and programming of the motors that would be used for the deployment routine, creating an adaptive optical element for the system with an applicable controls routine to maintain alignment of the system, and constructing and testing the system to confirm the predicted performance.

References

[1]   Telescope timeline - significant events in telescope history. Timeline of

Telescopes Significant Events for Telescopes. (n.d.).

http://www.historyoftelescope.com/telescope history/telescope-timeline/

[2]   Neugebauer, G., Habing, H. J., van Duinen, R., et al. 1984, ApJ, 278, L1

[3]   Houck, J. R., Soifer, B. T., Neugebauer, G., et al. 1984, ApJ, 278, L63

[4]   Fazio, G. G., Hora, J. L., Allen, L. E., et al. 2004, ApJS, 154, 10

[5]   Onaka, T., Matsuhara, H., Wada, T., et al. 2007, PASJ, 59, S401

[6]   Duval, V. G., Irace, W. R., Mainzer, A. K., & Wright, E. L. 2004, Proc. SPIE,

5487, 101

[7]   Rivta A. Keski-Kuha, Charles W. Bowers, et al. (2012). James Webb Space

Telescope optical telescope element mirror coatings. Space Telescopes and

Instrumentation 2012: Optyical, Infrared, and Millimeter Wave, 8442(2912), 84422J – 1

to 84422J – 12. https://doi.org/10.1117/12.925470

[8]   Park, Woojin, et al. "Development of linear astigmatism free—three mirror

system (LAF TMS)." Publications of the Astronomical Society of the Pacific 132.1010

(2020): 044504.

[9]   Han, W., Lee, D.-H., Jeong, W.-S., et al. 2014, PASP, 126, 853

[10]   Ree, C. H., Park, S.-J., Moon, B., et al. 2010, Proc. SPIE, 7731, 77311X

[11]   Seunghyuk Chang, "Elimination of linear astigmatism in off-axis three-mirror telescope and its applications," Proc. SPIE 8860, UV/Optical/IR Space Telescopes and Instruments: Innovative Technologies and Concepts VI, 88600U (26 September 2013); https://doi.org/10.1117/12.2023433

[12]   Neutrino QX, FLIR. Retrieved November 07, 2023. Available From: https://www.flir.com/products/neutrino-performance-series/?vertical=mwir&segment=oem

[13]   Wang, Q., Cheng, D., Wang, Y., Hua, H., & Jin, G. 2013, ApOpt, 52, C88

[14]   Kim, S., Pak, S., Chang, S., et al. 2010, JKAS, 43, 169

[15]   Chang, S. 2019, Optical Design and Fabrication (Freeform, OFT), FM2B, 6

[16]   R. E. Fischer, B. Tadic-Galeb, P. R. Yoder. Optical system design, McGraw-Hill Education, 2008. pp 49-54

[17]   J. E. Greivenkamp. Field guide to geometrical optics, SPIE, FG01, 2004, Page 89

[18]   Guenther, Bob D, and Duncan Steel. Encyclopedia of Modern Optics. Vol. 1-5. San Diego: Elsevier Science & Technology, 2018, pp 33.

[19]   Guenther, Bob D, and Duncan Steel. Encyclopedia of Modern Optics. Vol. 1-5. San Diego: Elsevier Science & Technology, 2018, pp 75.

[20]   Guenther, Bob D, and Duncan Steel. Encyclopedia of Modern Optics. Vol. 1-5. San Diego: Elsevier Science & Technology, 2018, pp 89-90.

[21]   R. E. Fischer, B. Tadic-Galeb, P. R. Yoder. Optical system design, McGraw-Hill Education, 2008, pp 638.

[22]   R. E. Fischer, B. Tadic-Galeb, P. R. Yoder. Optical system design, McGraw-Hill Education, 2008, pp 676-677.

[23]   R. E. Fischer, B. Tadic-Galeb, P. R. Yoder. Optical system design, McGraw-Hill Education, 2008, pp 678.

[24]   McElwain, Michael W., et al. "The James Webb Space Telescope Mission: Optical Telescope Element Design, Development, and Performance." Publications of the Astronomical Society of the Pacific 135.1047 (2023): 058001.

[25]   Tran, Ahn N. "James Webb Space Telescope Deployment Brushless DC Motor Characteristics Analysis." 43rd Aerospace Mechanisms Symposium. 2016.

[26]   Orbit Webb/NASA, et al. "James Webb Space Telescope". (n.d.). Retrieved November 13, 2023, from https://webb.nasa.gov/content/about/orbit.html.

[27]   Ewan S. Douglas, Greg Aldering, et al. (2023). Approaches to Lowering the Cost of Large Space Telescopes. Astronomical Optics: Design, Manufacture, and Test of Space and Ground Systems IV, 12677. https://doi.org/10.1117/12.2677843

[28]   L Spitzer, Jr. (1979). History of the Space Telescope. Quarterly Journal of the Royal Astronomical Society, 20, 29–36.

[29]   Z. Zheng, X. Liu, H. Li, and L. Xu, "Design and fabrication of an off-axis see-through head-mounted display with an x–y polynomial surface," Appl. Opt. 49, 3661-3668 (2010).

[30]   Observatory: Webb's Mirrors. (n.d.). James Webb Space Telescope: Goddard Space Flight Center. Retrieved November 9, 2023, Available from: https://webb.nasa.gov/content/observatory/ote/mirrors/index.html#5.